Tesi doctoral presentada per En/Na

Marc PERA TITUS

amb el títol

"Preparation, characterization and modeling of zeolite NaA membranes for the pervaporation dehydration of alcohol mixtures"

per a l'obtenció del títol de Doctor/a en

QUÍMICA

Barcelona, 29 de maig del 2006

Facultat de Química
Departament d'Enginyeria Química

UNIVERSITAT DE BARCELONA

This chapter deals with the study of the adsorption equilibrium of gases and vapors in zeolites. Section VII.1 includes the experimental results concerning the unary and binary adsorption isotherms of water and ethanol vapors on zeolite NaA commercial powder together with the fittings of several adsorption isotherms. Moreover, this section shows that the Adsorbed Solution formalism is a good tool for modeling binary adsorption isotherms of water and ethanol on zeolite NaA powder in terms of surface potential.

On the other hand, section VII.2 provides a new insight into the thermodynamics of the equilibrium gas adsorption process on microporous materials by using the general concepts in solution thermodynamics (3D) instead of surface adsorption thermodynamics (2D). In this section, a new adsorption isotherm is presented that includes the contribution of only two parameters that account for the two major aspects in the adsorption process: (1) the physical structure of the adsorbent, and (2) the adsorbent-adsorbate interaction.

VII.1. ADSORPTION EQUILIBRIUM OF WATER AND ETHANOL IN ZEOLITE NaA POWDER

VII.1.1. Characterization of the zeolite NaA (4A) commercial powder

The XRD pattern of the zeolite A commercial powder used in this study is shown in Figure VII.1. As can be seen, the solid was quite crystalline, being zeolite NaA the main species detected. $Ca(OH)_2$ was also found, but at very small quantities. The composition of the zeolite NaA powder was found to be >99.5 wt.%. The quantification of other minor elements contained in the solid reagent was done by XRF, which rvealed the presence of S, Ca, Mg and Fe, all of them as trace elements. Therefore, the solid could be regarded as highly pure.

The main physical properties of the zeolite NaA commercial powder used in this work are summarized in Table VII.1. As can be seen, the apparent density was found to be 2.01 g cm^{-3}, which is very close to the value reported in the literature, 2.00 g cm^{-3}. The mean size of the zeolite NaA particles was 2.08 μm with a narrow log-normal particle size distribution (see Figure VII.2). Moreover, the pore size distribution of the commercial particles (not shown) was determined from a N_2 adsorption isotherm at 77 K by means of the BET technique. All the pores lie in a narrow microporous range 0.40-0.50 nm, which approaches the value of 0.41 nm reported in the literature for this zeolite.

Finally, the SEM micrographs of some zeolite NaA commercial particles are displayed in Figure VII.3. First, some agglomerates of a size around 15 μm built of smaller zeolite NaA single crystals can be observed in Figures VII.3a-b. The inspection of the zeolite NaA single

single crystals (see Figures VII.3c-d) show the presence of truncated-side cubic crystals typical of zeolite NaA with a size in the range 1-2 μm. In fact, this size is in agreement with the mean crystal size determined by photon correlation spectroscopy (PCS) (see Table VII.1).

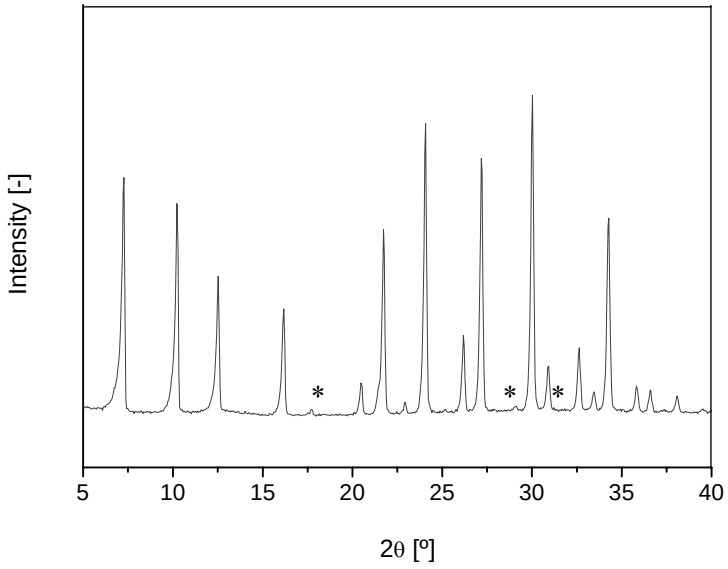

Figure VII.1: XRD pattern of the commercial zeolite NaA powder. All the peaks correspond to zeolite NaA, except for those marked with an asterisk, which refer to portlandite phase, $Ca(OH)_2$.

Table VII.1: Physical properties of the zeolite A commercial powder

Physical property	***Value***
Density [1] (apparent) [g cm^{-3}]	2.01
Particle size [2] (mean) [μm]	2.08
Particle size [2] (90% of area occupied) [μm]	3.22
BET specific surface [3] [m^2 g^{-1}]	255
Pore volume [3] [cm^3 g^{-1}]	0.100
Pore size [3] (mean) [nm]	0.41

[1] Determined by an He picnometer
[2] Determined by photon correlation spectroscopy
[3] Determined from a N_2 adsorption isotherm at 77 K by the BET technique

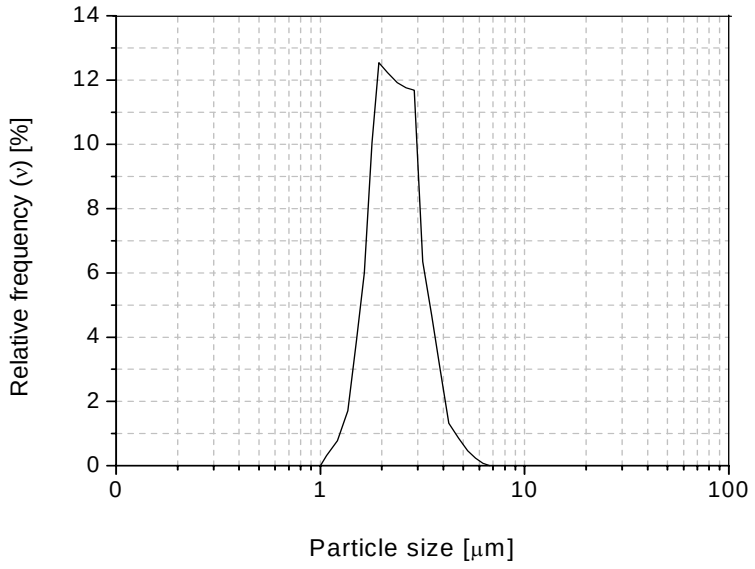

Figure VII.2: Particle size distribution (normalized) of the zeolite NaA commercial powder analyzed by photon correlation spectroscopy (PCS).

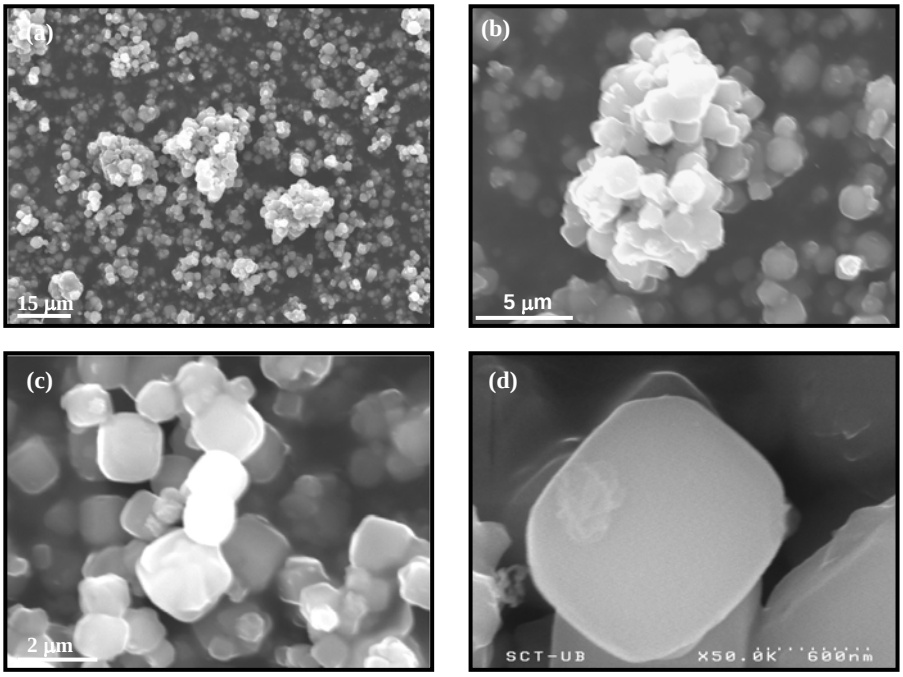

Figure VII.3: SEM micrographs of (a) an agglomerate of zeolite NaA crystals, (b) magnification of (a), (c) zeolite NaA single crystals and (d) Magnification of (c) inspected by FESEM.

VII.1.2. Unary adsorption isotherms of water and ethanol on zeolite NaA

This section shows the unary adsorption isotherms of water and ethanol on zeolite NaA commercial powder obtained in a microbalance (TGA) and from breakthrough curve analysis by mass spectrometry. For further details concerning the setup and experimental procedure of both methods see sections III.3.1 and III.3.2. The experimental conditions explored in the determination of the adsorption isotherms are summarized in Table VII.2. The reproducibility of the experimental data obtained by both experimental methods was determined by repeating some experiments at identical conditions at least three times. For both methods, the experimental error was found to be up to 15% (see section III.3.2.2).

Table VII.2: Experimental conditions tested for the determination of unary isotherms of water and ethanol on zeolite NaA commercial powder.

Physical property	*Range*
T [K]	305 – 423
Vapor pressure [Pa]	70 – 2400
N_2 flow rate [mL(STP) min^{-1}]	200

Figures VII.4a and VII.4b plot the unary adsorption isotherms of water and ethanol on zeolite NaA for the temperature range 305-423 K. As can be seen in Figure VII.4a, the experimental trends obtained for water loading with water partial pressure by using both experimental methods are in fairly good agreement, which verifies their reliability. The form of the isotherms of water and ethanol on zeolite NaA powder is characterized by a sharp increase in the molar loading at partial pressures <130 Pa, while it tends asymptotically to the saturation value, q_M, as the partial pressure approaches the saturation vapor pressure, P_i^o. It should be emphasized that the form of the isotherm approaches to that obtained for the adsorption isotherm of N_2 at 77 K on zeolite NaA powder (Type I isotherm according to the Emmett-Teller classification).

Moreover, following the general ideas outlined in section I.3.6.1, the experimental unary adsorption data for both water and ethanol were fitted to the single-site Langmuir (Eq. I.7), Freundlich (Eq. I.8) and Tóth (Eq. I.9) isotherms. A least-square non-linear optimization method, based on the Levenberg-Marquardt algorithm, was used to fit the parameters in Eqs. I.7-I.9 by comparison of predicted and experimental adsorption data. In the fitting process, the adsorption constant, $\mathbf{K_i}$ [kPa^{-1}], in Eqs. I.7 and I.9 and constant $\mathbf{K_{f,i}}$ [mol kg^{-1} $Pa^{-1/n}$] in Eq. I.8 were expressed by Eqs. VII.1 and VII.2

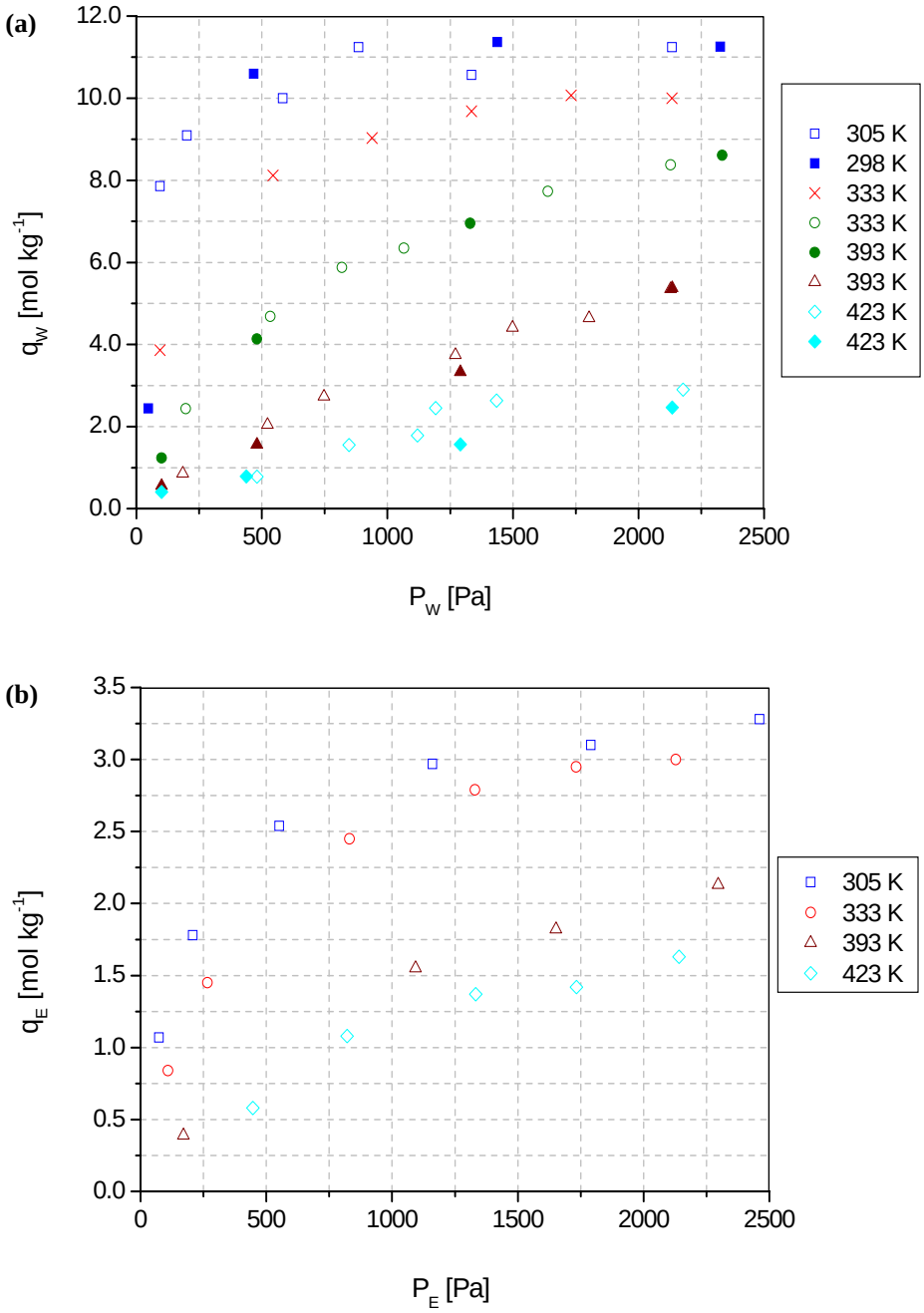

Figure VII.4: Adsorption isotherms of (a) water vapor and (b) ethanol vapor on zeolite NaA powder. Conditions as in Table VII.2. Open symbols correspond to the values determined from breakthrough curve analysis by mass spectrometry, while close symbols were obtained in the microbalance (TGA). Experimental error <15% for all the experiments.

$$K_i(T) = K_i(T_M)\exp\left[-\frac{\Delta H_i^o}{R}\left(\frac{1}{T}-\frac{1}{T_M}\right)\right] \quad \text{(Eq. VII.1)}$$

$$K_{f,i}(T) = K_{f,i}(T_M)\exp\left[-\frac{\Delta H_i^o}{R}\left(\frac{1}{T}-\frac{1}{T_M}\right)\right], \quad \text{(Eq. VII.2)}$$

where $\mathbf{T_M}$ is the mean temperature of the experimental series [K]. It should be noted that, in the present formulation, the saturation loading of each adsorbate, $q_{M,i}$, is assumed not to depend on the temperature, that is, the atomic distances between the atoms in the framework are assumed not to be altered by temperature. This assumption is usually accepted by many authors when modeling the adsorption of gases and vapors on zeolite NaA for temperatures <473 K (see for instance *Zhu et al., 2005*).

In Figures VII.5a and VII.5b both experimental unary adsorption loadings of water and ethanol obtained in the experimental conditions outlined in Table VII.2 are compared to adsorption loadings adjusted, respectively, to the different adsorption models proposed in this section. In addition, the statistics of the fittings and the values of the adjusted parameters are summarized, respectively, in Tables VII.3 and VII.4. For both species, the best fittings are obtained for the Langmuir and Tóth isotherms. Although the Tóth isotherm provides slightly better fittings than the Langmuir isotherm in terms of the sum of squares (SQ) and correlation coeficient (r^2), the former includes one additional parameter and the typical error of the parameters is somewhat higher.

Furthermore, when more than two parameters are involved, it is worth discussing the correlation between them. Tables VII.5 and VII.6 show the correlation matrixes for the estimated parameters for both water and ethanol, respectively, using the single-site Langmuir and Tóth isotherms. According to Table VII.5, it can be deduced that the correlation between the parameters in the single-site Langmuir isotherm is not a serious problem for both species, because the values of the matrixes are less than 0.95 (absolute value). However, according to Table VII.6, a higher correlation is observed for the pairs $K_w(T_M)$ and δ_w, and $K_E(T_M)$ and δ_E, for water and ethanol, respectively, in the fittings to the Tóth isotherm. Therefore, according to the statistics of the fittings, the single-site Langmuir isotherm was chosen as the adsorption model for both water and ethanol on zeolite NaA powder. It should be noted that the single-site Langmuir isotherm was also reported by *Breck (1984)* to describe the adsorption of water vapor on zeolite NaA. Finally, Figures VII.6 and VII.7 plot, respectively, the fitted trends of water and ethanol loadings with the partial pressure for the range of experimental conditions indicated in Table VII.2. The optimal parameters for the single-site Langmuir isotherm for both water and ethanol are described, respectively, by Eqs. VII.3 and VII.4

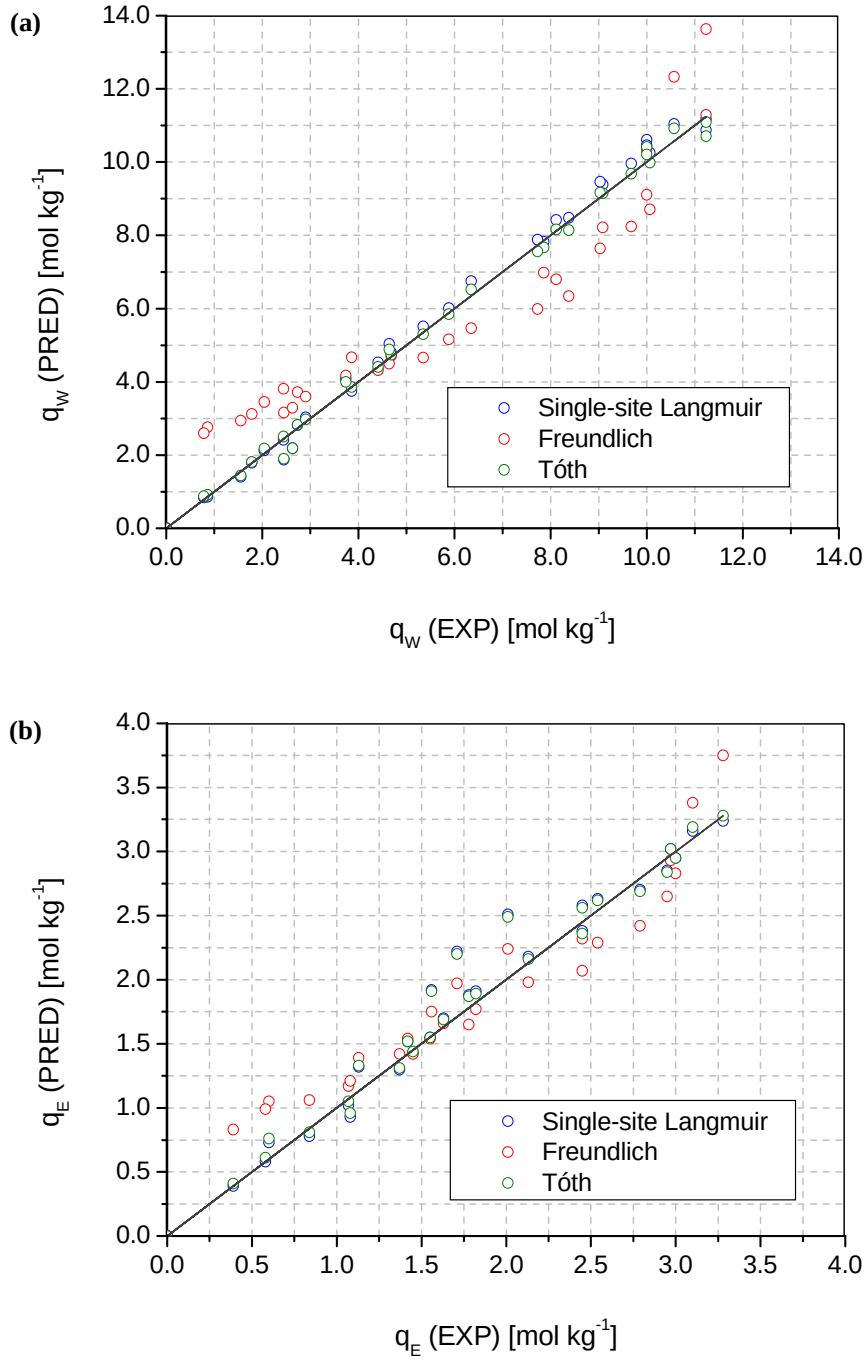

Figure VII.5: Comparison between experimental and fitted trends for (a) water and (b) ethanol loadings. Experimental conditions as in Table VII.2.

Table VII.3: Results of the fittings to the adsorption models listed in Table VII.3

Species	*Adsorption model*	*Sum of squares (SQ) [mol kg^{-1}] **	*Coef. Correlation (r^2) [-] **
Water	Langmuir	1.73	0.9985
	Freundlich	45.78	0.9678
	Tóth	1.50	0.9990
Ethanol	Langmuir	0.66	0.9939
	Freundlich	1.62	0.9852
	Tóth	0.58	0.9947

* T_M = 363.4 K

Table VII.4: Parameters fitted to the single-site Langmuir and Tóth isotherms

	Single-site Langmuir isotherm		*Tóth isotherm*	
Species	*Parameter* [1]	*Adjusted value* [2]	*Parameter* [1]	*Adjusted value* [2]
Water	ΔH_w^o [kJ mol^{-1}]	-45 ± 2	ΔH_w^o [kJ mol^{-1}]	-45 ± 2
	ΔS_w^o [J mol^{-1} K^{-1}]	-138 ± 1	ΔS_w^o [J mol^{-1} K^{-1}]	-108 ± 2
	$K_w(T_{ref})$ [kPa^{-1}]	1.4 ± 0.1	$K_w(T_{ref})$ [kPa^{-1}]	1.6 ± 0.3
	$q_{M,w}$ [kPa^{-1}]	11.4 ± 0.2	$q_{M,w}$ [kPa^{-1}]	11.4 ± 0.4
			δ_w [-]	0.87 ± 0.11
Ethanol	ΔH_E^o [kJ mol^{-1}]	-23 ± 2	ΔH_E^o [kJ mol^{-1}]	-24 ± 3
	ΔS_E^o [J mol^{-1} K^{-1}]	-78 ± 2	ΔS_E^o [J mol^{-1} K^{-1}]	-54 ± 3
	$K_E(T_{ref})$ [kPa^{-1}]	1.2 ± 0.2	$K_E(T_{ref})$ [kPa^{-1}]	1.6 ± 0.6
	$q_{M,E}$ [kPa^{-1}]	3.4 ± 0.2	$q_{M,E}$ [kPa^{-1}]	3.9 ± 0.7
			δ_E [-]	0.72 ± 0.26

[1] T_M = 363.4 K

[2] Confidence interval for probability level of 95%

H_2O: $$K_w(T) = (1.5 \pm 0.1)\exp\left[\frac{(45 \pm 2)1000}{8.314}\left(\frac{1}{T} - \frac{1}{363.4}\right)\right] \text{ [kPa}^{-1}\text{]} \qquad \text{(Eq. VII.3)}$$

EtOH: $$K_E(T) = (1.2 \pm 0.2)\exp\left[\frac{(23 \pm 2)1000}{8.314}\left(\frac{1}{T} - \frac{1}{363.4}\right)\right] \text{ [kPa}^{-1}\text{]} \qquad \text{(Eq. VII.4)}$$

It should be noted that the entropies of adsorption computed from the fitted adsorption constants at T_M = 363.4 K using the single-site Langmuir isotherm show values of -138 ± 1

and -78 ± 2 J mol^{-1} K^{-1} for both water and ethanol, respectively. As expected, the entropies show negative values.

Table VII.5: Correlation matrixes of the estimated parameters for water adsorption using the single-site Langmuir isotherm: (a) water vapor and (b) ethanol

(a)

	$K_w(T_M)$	ΔH_w^o	$q_{M,w}$
$K_w(T_M)$	1	-0.495	-0.795
ΔH_w^o	-0.495	1	0.522
$q_{M,w}$	-0.795	0.522	1

(b)

	$K_E(T_M)$	ΔH_E^o	$q_{M,E}$
$K_E(T_M)$	1	-0.348	-0.870
ΔH_E^o	-0.348	1	0.417
$q_{M,E}$	-0.870	0.417	1

Table VII.6: Correlation matrix of the estimated parameters for water adsorption using the single-site Langmuir isotherm: (a) water vapor and (b) ethanol

(a)

	$K_w(T_{ref})$	ΔH_w^o	$q_{M,w}$	δ_w
$K_w(T_M)$	1	-0.718	0.439	-0.896
ΔH_w^o	-0.718	1	-0.144	0.590
$q_{M,w}$	0.439	-0.144	1	-0.756
δ_w	-0.896	0.590	-0.756	1

(b)

	$K_E(T_{ref})$	ΔH_E^o	$q_{M,E}$	δ_E
$K_E(T_M)$	1	-0.262	0.576	-0.837
ΔH_E^o	-0.262	1	0.163	0.038
$q_{M,E}$	0.576	0.163	1	-0.922
δ_E	-0.837	0.038	-0.922	1

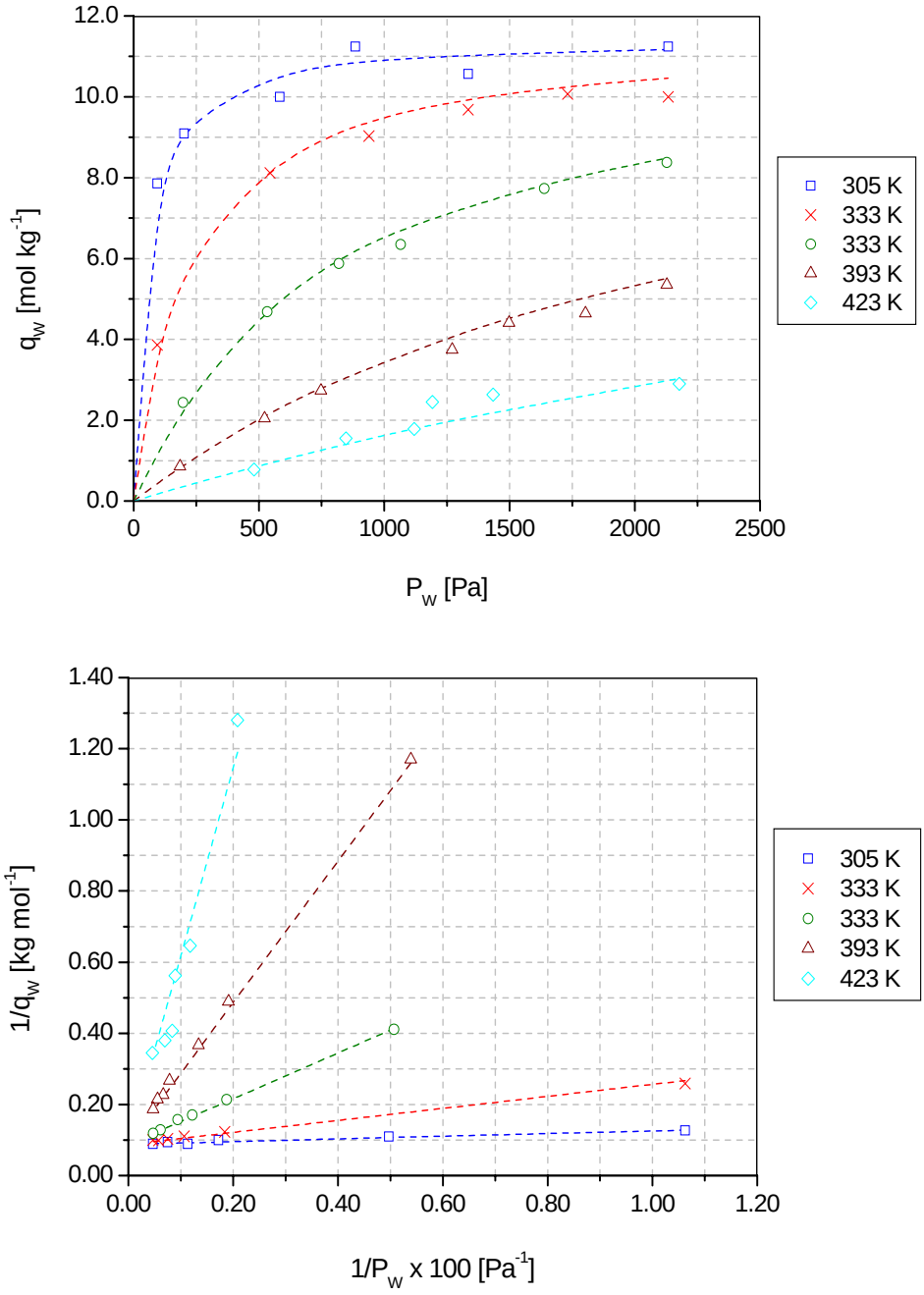

Figure VII.6: Adsorption isotherms of water vapor on zeolite NaA powder determined from breakthrough curve analysis by mass spectrometry. Evolution of (a) water loading with water partial pressure, and (b) the inverse of water loading with the inverse of water partial pressure. The dashed lined refer to the fittings Eq. I.7 (single-site Langmuir isotherm).

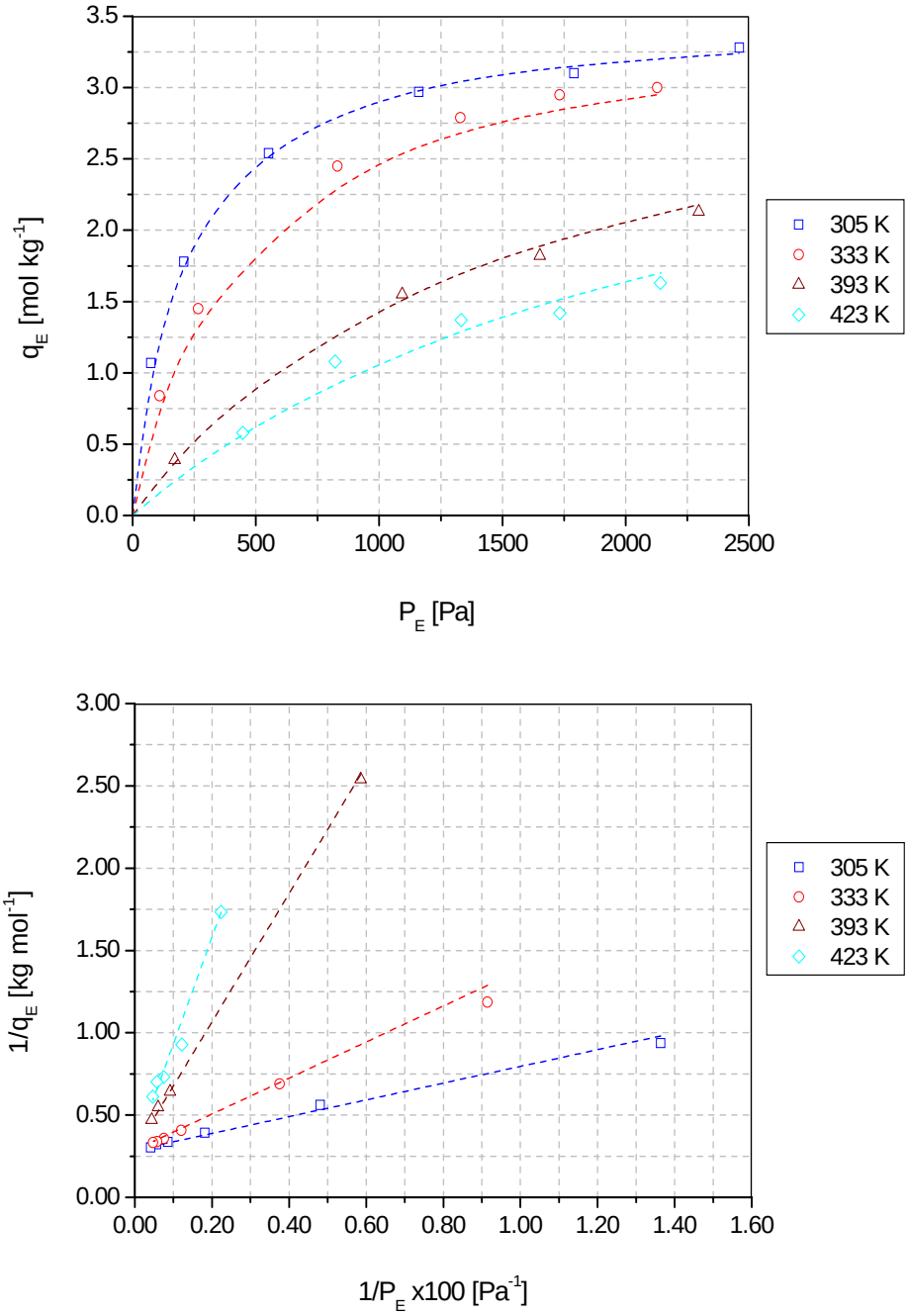

Figure VII.7: Adsorption isotherms of ethanol vapor on zeolite NaA powder determined from breakthrough curve analysis by mass spectrometry. Evolution of (a) ethanol loading with ethanol partial pressure, and (b) the inverse of ethanol loading with the inverse of ethanol partial pressure. The dashed lines refer to the fittings Eq. I.7 (single-site Langmuir isotherm).

On the other hand, the parameters obtained from the fittings to the single-site Langmuir isotherm for the unary adsorption of water and ethanol vapors on zeolite NaA powder are compared with literature data in Table VII.7. As can be seen, for water adsorption, although the molar saturation loading is slightly lower than the values reported in the literature, both the enthalpy of adsorption and the adsorption constant at 341 K show values of the same order of magnitude. Furthermore, the molar saturation loading of ethanol on zeolite NaA powder resembles to the value reported by *Okamoto et al. (2001)* using a volumetric method.

Table VII.7: Survey of literature data for water vapor adsorption on zeolite NaA

Species	$q_{M,w}$ ***[mol kg^{-1}]***	ΔH^{o}_{w} [kJ mol^{-1}]	K_w [kPa^{-1}]	***Method***	***References***
Water	15.8	-61 to -46 [1]	4.7 [2]	TEOM	Zhu et al. (2005)
	13.6	-	-	OBMC simulation [3]	Furukawa et al. (2004)
	15.0	-	-	Volumetric (vapor)	Okamoto et al. (2001)
	14.4	-	-	Volumetric (liquid)	Shah et al. (2000)
	-	-56	-	Microbalance (TGA)	Muller et al. (1998)
	13.9	-	-	Volumetric (vapor)	Breck (1984)
	11.4	**-45**	**3.6** [2]	**Breakthrough curve**	**This study**
Methanol	6.2	-	-	Volumetric (vapor)	Okamoto et al. (2001)
ethanol	3.7	-	-	OBMC simulation [3]	Furukawa et al. (2004)
	4.0	-	-	Volumetric (vapor)	Okamoto et al. (2001)
	3.4	**-23**	**2.2** [2]	**Breakthrough curve**	**This study**

[1] Isosteric value calculated from DSC from zero coverage to a saturated state

[2] Determined at 341 K

[3] Orientational-Bias Monte Carlo

Finally, regarding the values obtained for the molar saturation loadings of both water and ethanol vapors on zeolite NaA, it should be stressed that the ratio of their values expressed in mass units, Q_i [g / g ZA], approaches to the ratio of liquid densities of both water and ethanol (i.e. $Q_w/Q_E = (q_{M,w}/q_{M,E})\ (M_w/M_E) = 1.28 \rightarrow (\rho_w/\rho_E) = 1.37$). Therefore, the Gurvich's rule appears to be fulfilled for this system. This result supports the idea that the unary adsorption of water and ethanol on zeolite NaA does not only obey to their affinity for zeolite NaA, which is actually included in the adsorption constant, but also to size entropy effects, which are included in the molar saturation loading. Because the kinetic diameter of water (0.29 nm) is much lower than that of ethanol (0.43 nm), a higher number of water molecules can adsorb on zeolite NaA, thus resulting in a higher adsorption of water than ethanol.

VII.1.3. Prediction of binary adsorption isotherms of water and ethanol in zeolite NaA powder

This section shows the experimental results and modeling of the simultaneous adsorption process of water and ethanol in zeolite NaA powder. The general concepts used in solution thermodynamics are extended in this section to account for the prediction of the experimental trends for the ethanol/water binary system from unary adsorption data presented in section VII.1.3 through the use of the so-called Ideal Adsorbed Solution Theory (IAST) and Predictive Real Adsorbed Solution Theory (IAST).

VII.1.3.1. Ideal Adsorbed Solution Theory: preliminary simulations

The Ideal Adsorbed Solution Theory earlier proposed by *Myers and Prausnitz (1965)* reveals as a good tool to describe mixture adsorption, since it constitutes a thermodynamically consistent model compared with, for instance, the Extended single-site Langmuir isotherm, for species with different molar saturation loadings, $q_{M,i}$. The great advantage of this model relies on the possibility to predict multicomponent adsorption isotherms on microporous materials (e.g., zeolites) from unary adsorption isotherm data through the use of the concept of surface potential. Further modifications of the model such as the Predictive Adsorbed Solution Theory (PRAST) proposed *Sakuth et al. (1998)* allow to include the effect of non-ideality of the adsorbed phase in the prediction of multicomponent isotherms.

In the most general case where the effect of the non-ideality of the adsorbed phase is included in the modeling and that the single-site adsorption isotherm can be used to describe the unary adsorption of each species **i**, the multicomponent adsorption isotherm for N species can be obtained by solving the following set of equations (Eqs. VII.5)

$$P\,y_i = P_i^o(\Phi)\,\gamma_i(\Phi)\,x_i \qquad i = w, E \qquad \text{(Eqs. VIII.5)}$$

$$\sum_{i=1}^{N} y_i = \sum_{i=1}^{N} x_i = 1$$

$$-\frac{\Phi}{RT} = \int_0^{P^o(\Phi)} \frac{q_i^o(P_i)}{P_i}\,\delta P_i = q_{M,i}\,\mathrm{Ln}\left(1 + K_i\,P_i^o\right) \geq 0$$

where $\mathbf{y_i}$ and $\mathbf{x_i}$ are the molar fractions of species **i** in the gas and adsorbate phases [-], respectively, $\boldsymbol{\gamma_i(\Phi)}$ is the activity coefficient of species **i** in the adsorbate [-] (that can be calculated by the recipe provided Appendix C), P is the total pressure in the gas phase [kPa], and $\mathbf{P_i^o(\Phi)}$ is the adsorptive saturation pressure corresponding to the solution temperature and surface potential Φ. Moreover, the total loading of each species in the adsorbate can be determined, respectively, by the set of Eqs. I.31-I.33 (see section I.3.6.2). According to the set

of Eqs. VIII.5 and I.31-I.33, the ability of an adsorbent to adsorb selectively a species **i** with respect to the others in a gas or vapor mixture depends on the value of both its adsorption constant and molar saturation loading with respect to those ascribed to the rest of species. The effect of both parameters in the adsorption of a mixture of two species according to the IAST model is shown is Figures VII.8-VII.13. Figures VII.8-VII.10 show the effect of the ratio of adsorption constants ($K_1 : K_2$) of two species with equal molar saturation loadings ($q_{M,1} = q_{M,2} = 10$ mol kg^{-1}). As can be seen, as the ratio $K_1 : K_2$ increases, the solid tends to adsorb selectively species 1 instead of species 2, which implies an increase in the molar fraction of the former species in the adsorbed phase (see Figure VII.8) together with a raise of its loading on the solid compared to that of species 2 (see Figure VII.10). Moreover, for a given surface potential, higher $K_1 : K_2$ ratios implies that the adsorption occurs at higher adsorptive saturation pressures of species 2, P_2^o (see Figure VII.9).

On the other hand, Figures VII.11-VII.13 show the effect of the ratio of molar saturation loadings of two species ($q_{M,1} : q_{M,2}$) in the adsorption of two species with equal adsorption constants ($K_1 = K_2 = 3.75$ kPa^{-1}). As the ratio $q_{M,1} : q_{M,2}$ increases, the solid tends to adsorb selectively species 1 instead of species 2, which implies an increase in the molar fraction of the former species in the adsorbed phase (see Figure VII.11) together with a raise of its loading on the solid compared to that of species 2 (see Figure VII.13). Moreover, for a given surface potential, the adsorption occurs at higher adsorptive saturation pressures of species 2, P_2^o, for higher $q_{M,1} : q_{M,2}$ ratios (see Figure VII.12).

VII.1.3.2. Binary adsorption isotherms of water and ethanol on zeolite NaA

Figures VII.14 and VII.15 show the binary adsorption isotherms of water and ethanol on zeolite NaA powder obtained from breakthrough curve analysis at 333 K and 1.3 and 2.1 total vapor pressure according to the experimental procedure described in section III.3.2 and experimental conditions summarized in Table VII.8. Figure VII.14 shows the y – x diagram for the mixture under study. As can be seen, for both total vapor pressures, the adsorbed phase tends to be enriched with water as the water composition in the vapor phase increases. The experimental trend is predicted by both the IAST and PRAST models taking into account the experimental data for adsorption constants and molar surface saturation loadings for both species included in Table VII.9. For the latter model, the activity coefficients for the water/ethanol binary system have been estimated from surface activity coefficients at infinite dilution according to the procedure indicated in Appendix C. Although both models predict successfully well the experimental trends of the water composition of the adsorbed phase with that of the vapor phase, it seems that the latter provides slightly better predictions, since it includes the contribution of the non-ideality of the adsorbed mixture in the computations.

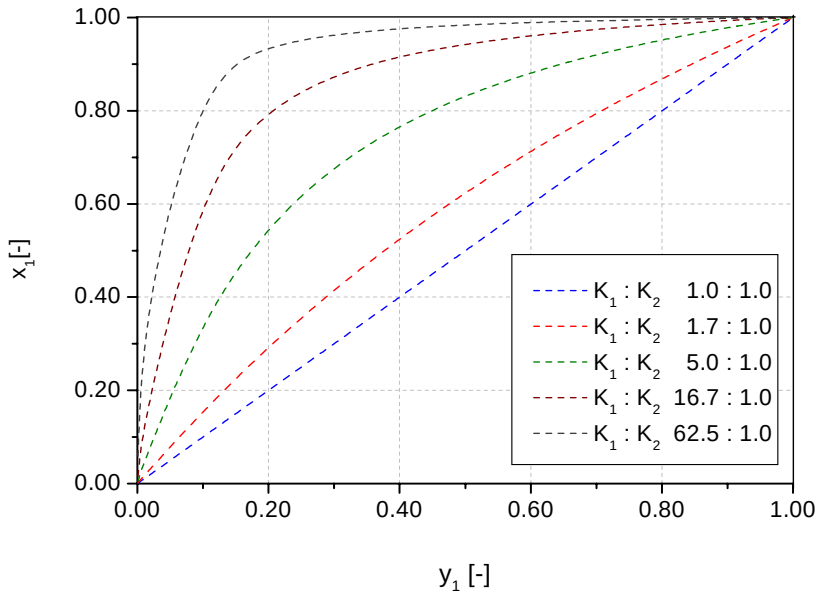

Figure VII.8: x – y equilibrium adsorption diagram according to the IAST model for two species with q_M = 10 mol kg^{-1} and K_1 = 3.75 kPa^{-1} for different ratios between the adsorption constants

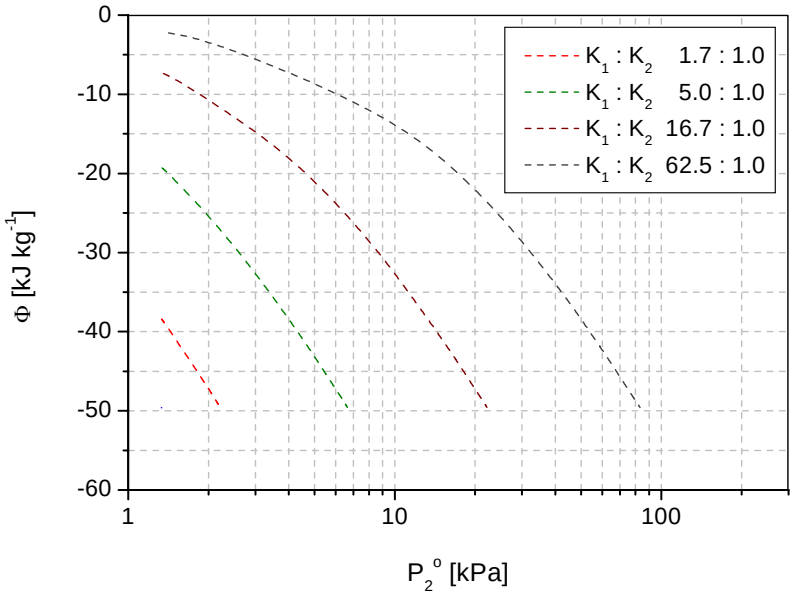

Figure VII.9: Surface potential vs. equilibrium adsorptive saturation pressure of species 2 according to the IAST model for two species with q_M = 10 mol kg^{-1} and K_1 = 3.75 kPa^{-1} for different ratios between the adsorption constants

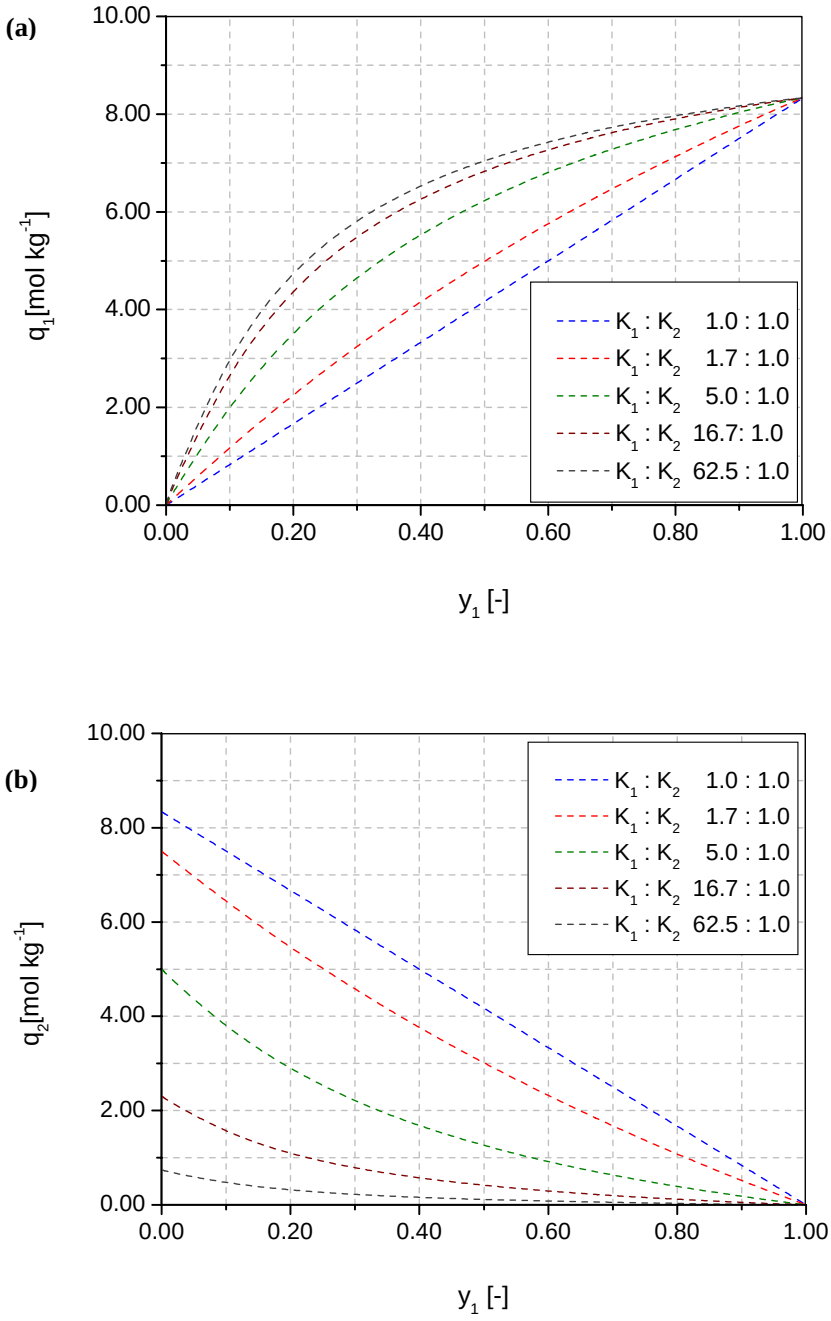

Figure VII.10: Molar loading of (a) species 1 and (2) species 2 with the molar fraction of species 1 in the gas phase according to the IAST model for two species with q_M = 10 mol kg^{-1} and K_1 = 3.75 kPa^{-1} for different ratios between the adsorption constants

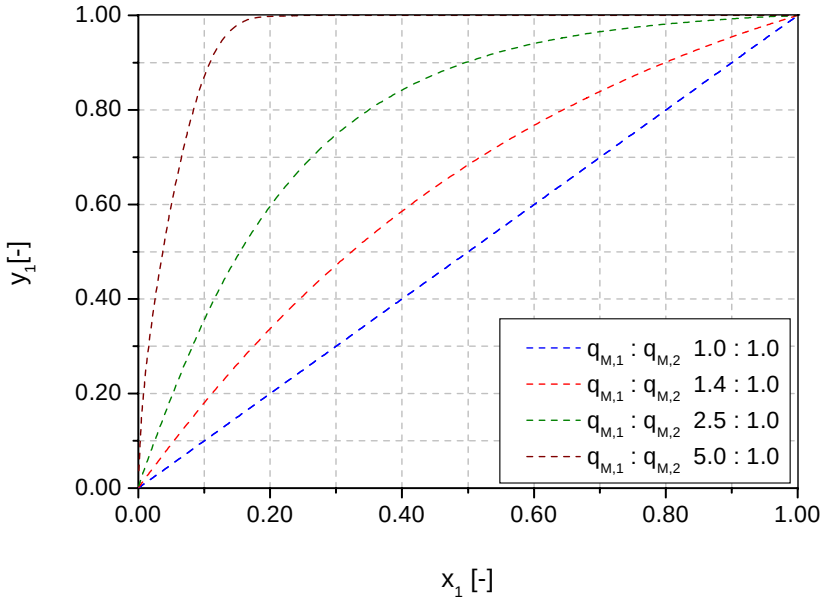

Figure VII.11: x – y equilibrium adsorption diagram according to the IAST model for two species with equal adsorption constants ($K_1 = K_2 = 3.75$ kPa^{-1}) and different $q_{M,1} : q_{M,2}$ ratios with $q_{M,1} = 10$ mol kg^{-1}

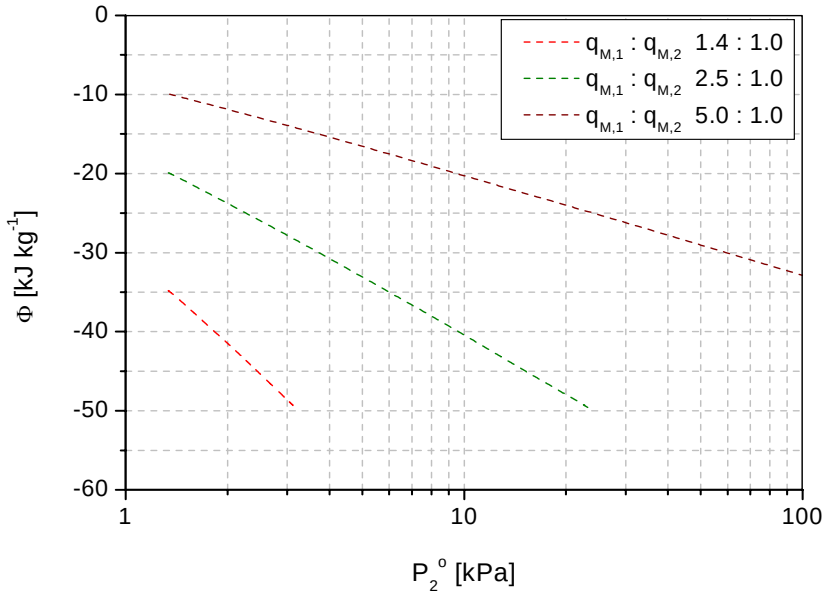

Figure VII.12: Surface potential vs. equilibrium adsorptive saturation pressure of species 2 according to the IAST model for two species with equal adsorption constants ($K_1 = K_2 = 3.75$ kPa^{-1}) and different $q_{M,1} : q_{M,2}$ ratios with $q_{M,1} = 10$ mol kg^{-1}

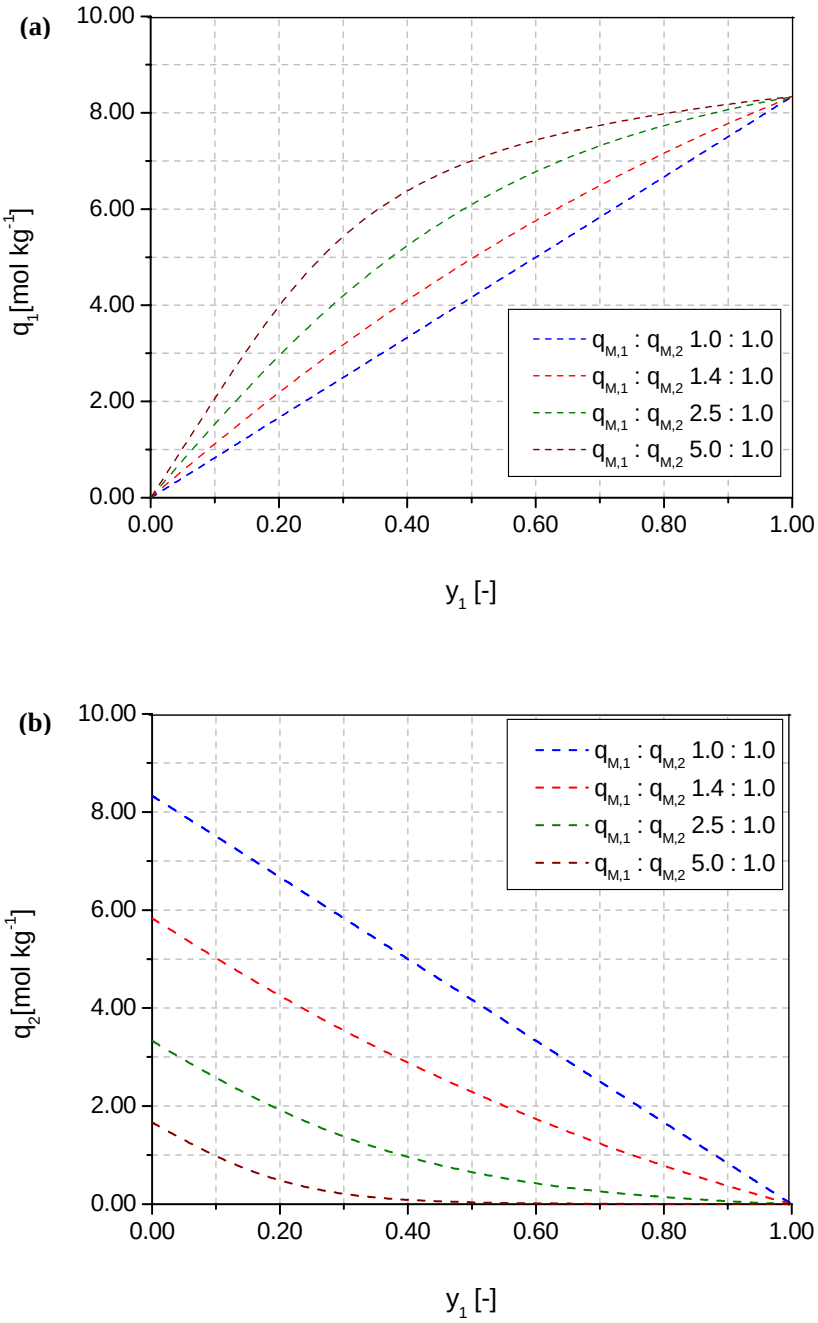

Figure VII.13: Molar loading of (a) species 1 and (2) species 2 with the molar fraction of species 1 in the gas phase according to the IAST model for two species with equal adsorption constants (K_1 = K_2 = 3.75 kPa^{-1}) and for different $q_{M,1}$: $q_{M,2}$ ratios with $q_{M,1}$ = 10 mol kg^{-1}

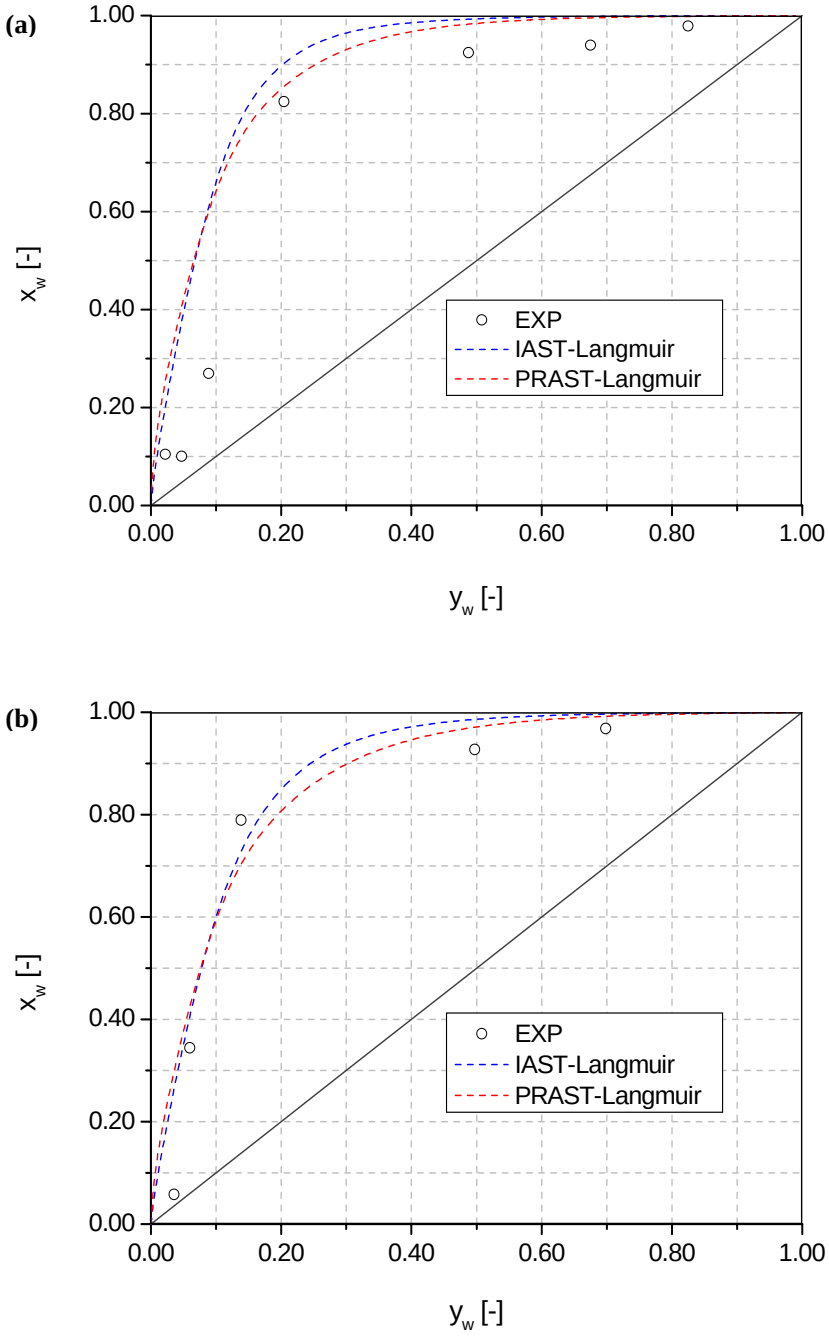

Figure VII.14: y – x diagram for water and ethanol adsorbed on zeolite NaA powder at 333 K and (a) 1.3 kPa and (b) 2.1 kPa total vapor pressure. The dashed lines correspond to the trends predicted by the IAST and PRAST models with the input unary adsorption data in Table VII.9.

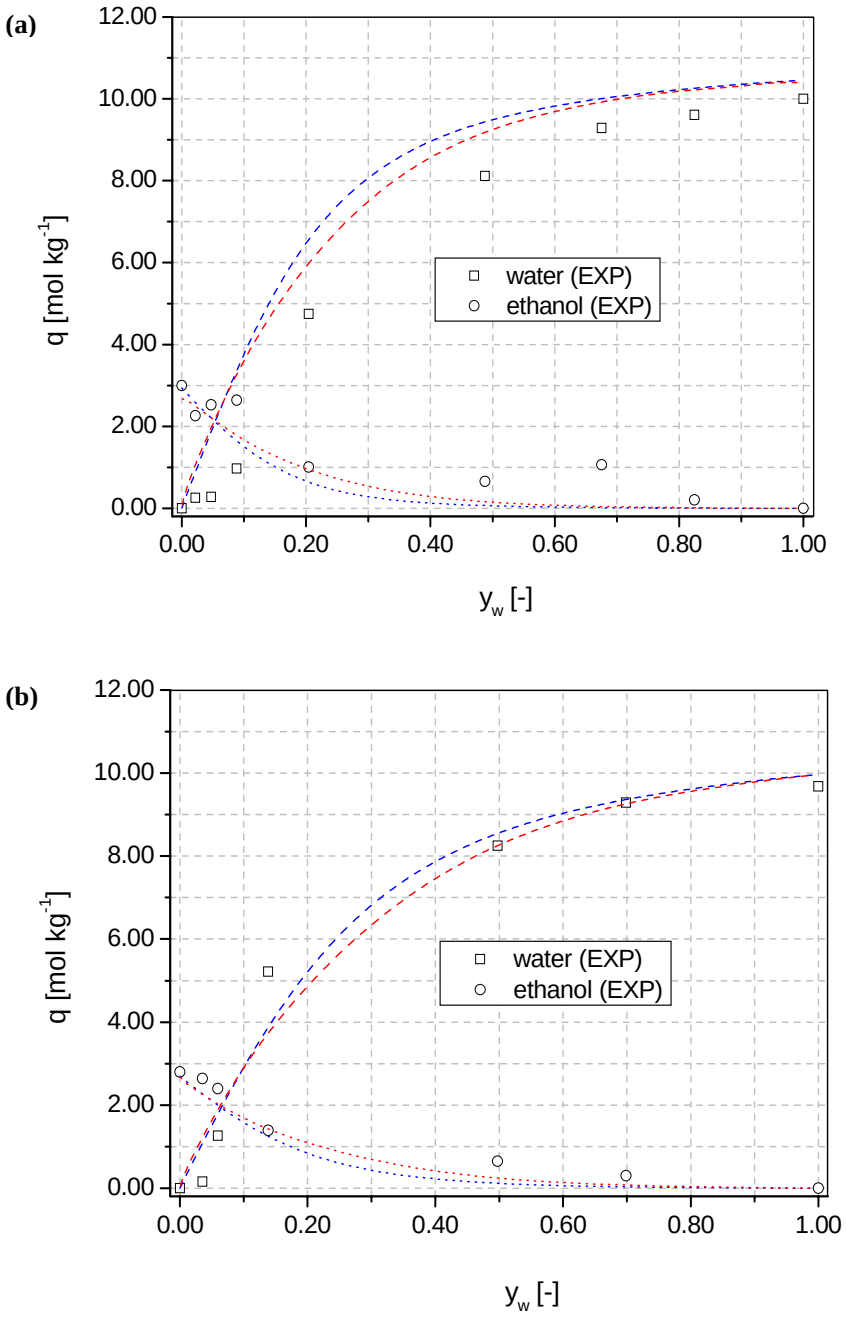

Figure VII.15: Evolution of water and ethanol loadings on zeolite NaA powder at 333 K and (a) 1.3 kPa and (b) 2.1 kPa total vapor pressure. The dashed and dotted lines correspond to the trends predicted by the IAST (blue) and PRAST (red) models with the input unary adsorption data in Table VII.9 for water and ethanol loadings, respectively.

Table VII.8: Experimental conditions tested for the determination of binary isotherms of water and ethanol on zeolite NaA commercial powder.

Physical property	*Value*
T [K]	333
Vapor pressure [Pa]	1300 – 2100
Water composition in the vapor phase (y_w) [mol%]	0 – 100
N_2 flow rate [cm^3 (STP) min^{-1}]	200

Table VII.9: Input data for the prediction of binary adsorption isotherms by IAST and PRAST models

Single-site unary adsorption data	*Value*
$q_{M,w}$ [mol kg^{-1}]	11.40
$q_{M,E}$ [mol kg^{-1}]	3.47
K_w [kPa^{-1}]	5.20
K_E [kPa^{-1}]	2.64

On the other hand, Figure VII.14 shows the evolution of the water and ethanol loadings with the water composition in the vapor phase. As can be seen, while the water loading tends to increase with the water composition, that of ethanol tends to decrease, in agreement with the positive trend observed for water composition in the adsorbed phase with respect to that in the vapor phase. The experimental trend outlined is predicted by both the IAST and PRAST models. The observed trends for water and ethanol loadings with vapor composition reinforce the idea put forward that zeolite NaA adsorbs selectively water with respect to ethanol on the grounds of its hydrophilic character. It should be emphasized that this hydrophilic character in not only due to the higher affinity of zeolite NaA for water than for ethanol, which is actually included in the adsorption constant, but also due to size entropy effects, which are included in molar saturation loadings. Because the kinetic diameter of water (0.29 nm) is much lower than that of ethanol (0.43 nm), a higher number of water molecules can be adsorbed on zeolite NaA, thus resulting in a higher adsorption of water than ethanol.

Figure VII.16 shows the evolution of the surface potential with the adsorptive saturation pressure of water and ethanol at 333 K and 1.3 and 2.1 kPa total vapor pressure. As can be seen, lower adsorptive saturation pressures are needed to reach a fixed value of surface

potential for water than for ethanol, which confirms the stronger adsorption of water than ethanol on zeolite NaA.

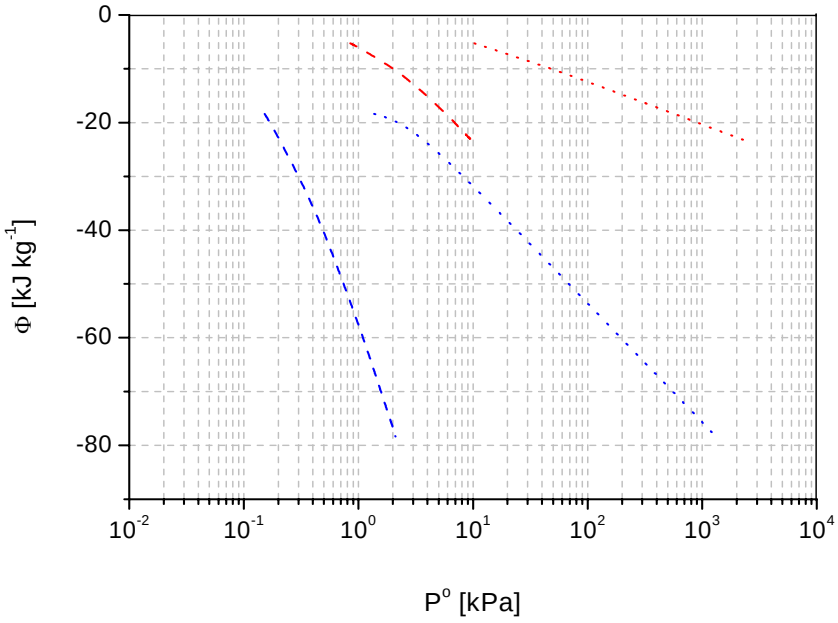

Figure VII.16: Evolution of the surface potential with the adsorptive saturation pressure for the adsorption of water and ethanol on zeolite NaA powder at 333 K and 1.3 kPa (red lines) and 2.1 kPa (blue lines) total vapor pressure. The dashed and dotted lines correspond to water and ethanol, respectively, predicted by the PRAST model with the input unary adsorption data in Table VII.9.

VII.2. POTENTIAL THERMODYNAMIC ISOTHERMS FOR MICROPOROUS MATERIALS (PTI). FORMULATION AND EXPERIMENTAL VALIDATION

In this section, a new general expression is presented that provides a thermodynamic description of the adsorption equilibrium of gases and vapors in **microporous** materials, which has been developed from the earlier ideas suggested by *Llorens (2005)*. This isotherm is based on a potential trend between the dimensionless integral free energy relative to saturation, **-Ψ/RT**, and parameter **Z=1/-Ln(Π)**, $\Psi/RT \propto Z^{-m}$, where **Π** is the reduced pressure, P/P^o [-], **θ** is the fractional occupancy [-], and **m** is a structural parameter that characterizes the adsorbent. This isotherm is termed as ***Potential Thermodynamic Isotherm (PTI)*** in the remainder of this section. In general terms, the contribution presented in this section relies on regarding the equilibrium adsorption in microporous materials as a 3D phenomenon instead of a classical surface (2D) process. The Dubinin-Astakhov and the generalized Langmuir isotherms are analyzed and rewritten in terms of the PTI. The former,

on the grounds of its 3D character, appears as a particular case of the PTI, while the generalized Langmuir isotherm, despite being widely used for describing the adsorption of gases and vapors in microporous materials (see for instance the results in section VII.1 for water and ethanol adsorption on zeolite NaA powder), shows characteristics of the PTI only for a slight range of values for its parameters.

VII.2.1. Potential thermodynamic isotherm (PTI)

Following the ideas underlined in section I.3.6.1, the integral free energy of an adsorbate for unary equilibrium adsorption of a condensable gas or vapor can be accounted for by Eq. VII.6 (Eq. I.26), which allows to obtain Eq. VII.7 (Eq. I.28) for the differential free energy if the adsorbate is regarded as a perfect gas

$$\Delta\overline{G}^{a} = q\left(\mu - \mu^{o}\right) + \Phi, \qquad \text{(Eq. VII.6)}$$

$$\Delta\overline{g}^{a} = RT\,Ln\left(\frac{P}{P^{o}}\right), \qquad \text{(Eq. VII.7)}$$

where Φ is again the surface potential [J kg of adsorbate^{-1}]. The maximum adsorption or saturation loading, q_M, is reached when the gas pressure approaches the saturation vapor pressure of the liquid adsorbate at temperature T, P^o, and the difference between the integral free energy at a particular state related to saturation, $\mathbf{Y}$ [J kg of adsorbent^{-1}], is expressed by Eq. VII.8

$$Y = \Delta\overline{G}^{a}\left(q_M\right) - \Delta\overline{G}^{a}\left(q\right) = \left[\overline{G}^{a}\left(q_M\right) - \overline{G}^{a}\left(q\right)\right] - \mu^{o}\left[q_M - q(P)\right] \qquad \text{(Eq. VII.8)}$$

which turns into Eq. VII.9 using Eq. VII.6

$$-Y = \left[\Phi(P) - \Phi\left(P^{o}\right)\right] - q(P)\left[\mu^{o} - \mu\right] \qquad \text{(Eq. VII.9)}$$

The integral free energy related to the saturation loading can be also calculated by Eq. VII.10

$$Y = \int_{q(P)}^{q_M} \Delta\overline{g}^{a}\,\delta q = RT\int_{q(P)}^{q_M} Ln\left(\frac{P}{P^{o}}\right)\delta q \qquad \text{(Eq. VII.10)}$$

The latter expression can be determined from the experimental adsorption isotherm, q(P). Eq. VII.10 can be rewritten in dimensionless form by Eq. VII.11

$$\frac{\Psi}{RT} = \int_{\theta}^{1} Ln(\Pi)\,\delta\theta, \qquad \text{(Eq. VII.11)}$$

where $\Psi=Y/q_M$ [J mol of adsorbate^{-1}]. As can be observed from Eq. VII.11, $\Psi/RT < 0$ for $\theta \to 0$, while $\Psi/RT \to 0$ for $\theta \to 1$, and its value becomes more negative as $\theta \to 0$.

It should be highlighted that the variable $Z = 1/-Ln(\Pi)$ evolves from 0 to infinite for adsorbate pressures going from 0 to P^o. For a great number of experimental gas adsorption data in meso- and microporous materials (*Jaroniec, 1995; Sahouli et al., 1996; Jaroniec et al., 1997; Wang and Li, 1997; Esquena et al., 2000; Terzyk and Gauden, 2003*), linear trends with negative slope are observed when representing $-\Psi/RT$ vs. **Z** in double logarithmic axes (see Figure VII.17). This relationship reflects that the adsorption process in porous materials shows fractal behavior (*Mandelbrot, 1988*). Furthermore, when $Z \to 0$ ($\Pi \to 0$ or $\theta \to 0$), $-\Psi/RT$ reaches its maximum value, $-\Delta G^a(q_M)/q_M\,RT$, which will be termed as G^o [-] in the remainder of this section. This value corresponds to the integral free energy of the adsorbed phase expressed in terms of RT at saturation loading. The mathematical function that relates $-\Psi/RT$ with Π in such a way that $-\Psi/RT \to G^o$ when $\Pi \to 0$ and $-\Psi/RT \propto Z^{-m}$ for higher values of Π (but always $\Pi \leq 1$) (potential trend or "scaling law" related to its fractal behavior) can be described by Eq. VII.12

$$-\frac{\Psi}{RT} = \int_\theta^1 -Ln(\Pi)\delta\theta = \frac{G^o}{1+k\left[\frac{1}{-Ln(\Pi)}\right]^m} = \frac{G^o}{1+k\,Z^m} \qquad \text{(Eq. VII.12)}$$

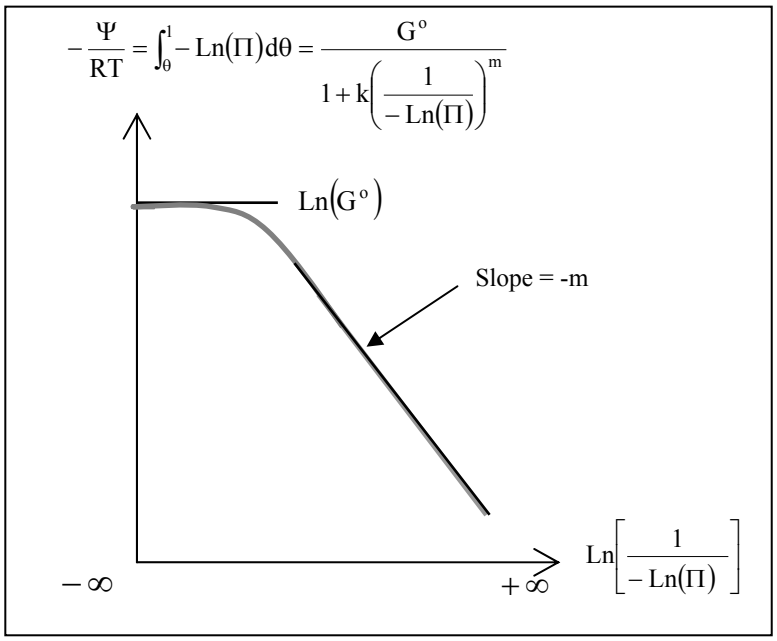

Figure VII.17: Representation of $-\Psi/RT$ vs. $Z = 1/-Ln(\Pi)$ in double logarithmic axes.

Eq. VII.12 is an isotherm that relates dimensionless variables with three dimensionless parameters: $\mathbf{G^o}$, **k** and **m**, each of which has a physical meaning. As it was aforementioned, $\mathbf{G^o}$ is the dimensionless integral free energy of the adsorbed phase at saturation loading. Moreover, **m** is the exponent that governs the evolution of the integral free energy along the adsorption process and that reflects its fractal behavior. For low values of **Z**, the adsorbate tends to adsorb at adsorbent positions where the adsorbate-adsorbent interaction is more energetic, while for higher values, it adsorbs at less energetic positions. The evolution of the integral free energy relative to saturation, $-\Psi/RT$, with **Z** also depends parameter **m**, which reflects the influence of the structure of the adsorbent in the adsorption process. Finally, parameter **k** can be related to the value $\Pi = \Pi_k$ [-], which is defined as the Π value that produces an adsorption whose adsorbed phase integral free energy equals $\mathbf{G^o/2}$. The value of Π_k can be related to **k** and **m** by Eq. VII.13

$$\Pi_k = \exp\left(-k^{1/m}\right) \qquad \text{(Eq. VII.13)}$$

Eq. VII.12 can be rewritten using parameter Π_k instead of parameter **k** by Eq. VII.14

$$-\frac{\Psi}{RT} = \int_\theta^1 -\mathrm{Ln}(\Pi)\,\delta\theta = \frac{G^o}{1+\left[\dfrac{\mathrm{Ln}(\Pi_k)}{\mathrm{Ln}(\Pi)}\right]^m} \qquad \text{(Eq. VII.14)}$$

It should be mentioned that the plateau zone of the isotherm ($-\Psi/RT = G^o$) cannot be easily observed because loadings at very low Π values ($<10^{-5}$) are extremely difficult to be experimentally determined. Figure VII.18 shows the adsorption isotherm of N_2 at 77 K for a reference zeolite (faujasite, zeolite X) analyzed at very low pressures by the Federal Institute for Materials Research (BAM, http://www.bam.de), where the beginning of plateau zone corresponding to the value of G^o can be observed for reduced pressures around 10^{-8} when expressing the isotherm in terms of Eq. VII.12.

On the other hand, in most of practical applications, only the potential zone can be distinguished for higher Π values, whose determination does not suffer from experimental limitations. This potential trend implies a linear correlation of $-\Psi/RT$ with Z in double logarithmic axes with slope **m** and with an integral free energy of the adsorbed phase G^o/k. For such a case, Eq. VII.12 reduces to Eq. VII.15

$$-\frac{\Psi}{RT} = \int_\theta^1 -\mathrm{Ln}(\Pi)\,\delta\theta = \frac{G^o}{k}\left[\frac{1}{-\mathrm{Ln}(\Pi)}\right]^{-m} = \frac{G^o}{k}\left[-\mathrm{Ln}(\Pi)\right]^m, \qquad \text{(Eq. VII.15)}$$

Comparing Eq. VII.15 with Eq. VII.9 and using the definition $\Psi = Y/q_M$:

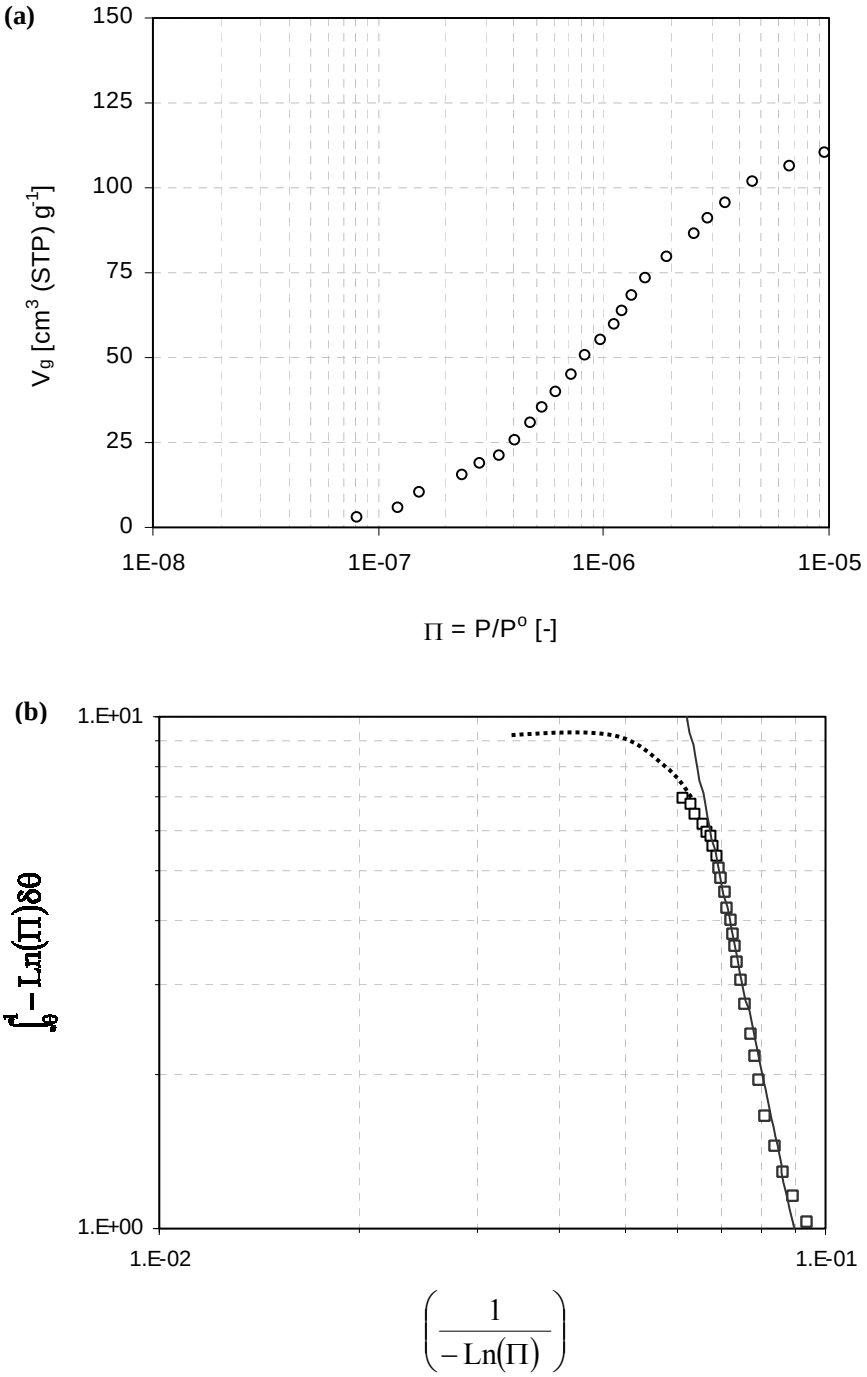

Figure VII.18: (a) adsorption isotherm of N_2 at 77 K for a reference zeolite analyzed at very low pressures by the Federal Institute for Materials Research and Testing (BAM, Unter den Eichen 87, 12205 Berlin, Germany), and (b) representation of the same isotherm in terms of Eq. VII.12. The dotted curve represents the extrapolation of the plateau region.

$$-\frac{\Psi}{RT}=-\left\{\frac{\left[\Phi\left(P^{o}\right)-\Phi(P)\right]}{RT}+\theta(P)\frac{\left[\mu^{o}-\mu\right]}{RT}\right\}\propto\left(\frac{1}{-Ln(\Pi)}\right)^{-m}$$

and $-\Psi/RT\rightarrow -G^{o}/k$ when $\Pi\rightarrow 1/e\approx 0.36788$, being **e** the base of natural logarithms.

According to Eq. VII.15, two aspects play a relevant role in the equilibrium adsorption process: (1) the adsorbate-adsorbent interaction, which depends on the chemical nature of both the adsorbate and the adsorbent, and (2) the energy distribution of this interaction, which depends on the physical structure of the adsorbent. It should be highlighted that, given an adsorbate and an adsorbent, despite being their interaction already determined, the same adsorbent material can show different physical structures in different samples. This information is included implicitly in parameter **m**. Furthermore, for different adsorbates, the energy distribution of the adsorbate-adsorbent interaction for a particular adsorbent should remain invariable and the adsorbent should keep the same value for parameter **m**. On the other hand, for a series o adsorbents that show the same chemical nature but different physical structure, the adsorbate-adsorbent interaction for a particular adsorbate should remain constant, which implies the same value for parameter $\mathbf{G^{o}}$. However, the energy distribution might change for each adsorbent, which would involve a change in the value of parameter **m**.

The meaning of parameter **m** according to Eq. VII.15 goes beyond the aforementioned general comments. The application of this isotherm to mesoporous materials with surfaces that show a fractal geometric structure, characterized by a surface fractal dimension, D_s, and under the point of view of surface thermodynamics (2D), $\mathbf{m} = D_s - 2$. In fact, **m** determines the fractal structure of the adsorbent with respect to the adsorption process irrespective of its surface nature (mesoporous materials) or volumetric (microporous materials). It should be noted that, for the special case of a surface, the curvature radii distribution of the surface rugosity is related to the energy distribution that rules the adsorption process. For this special case, the curvature radius is given by the Kelvin equation (Eq. I.3) and it is directly proportional to the value of **Z** (*Neimark, 1992*).

In the remainder of this section, Eq. VII.15 will be referred as ***Potential Thermodynamic Isotherm (PTI)*** and will be used as a general isotherm to characterize the adsorption of gases in microporous materials. This terminology is based on the idea that the parameters that appear in the isotherm have a thermodynamic meaning and that the difference in the integral free energy related to the saturation loading, $-\Psi/RT$, actually determines the adsorption process and shows a potential trend with Π in the pressure range at which adsorption occurs. Moreover, adsorption is also assumed to present fractal behavior with pressure, which is essentially different from the geometric fractal behavior in the 2D-space. Microporous materials are not expected to show geometric fractal behavior, since the pore size range is lower than a decade (that of pressure covers several decades).

VII.2.2. Comparison between the PTI and the Dubinin-Astakhov isotherm

The Dubinin-Astakhov isotherm relates the fractional occupancy of an adsorbate with its reduced pressure according to Eq. VII.16 (or I.14)

$$\mathrm{Ln}(\theta) = \mathrm{Ln}\left(\frac{q}{q_M}\right) = -\left[-\frac{RT}{E^o}\mathrm{Ln}(\Pi)\right]^{\alpha} \qquad \text{(Eq. VII.16)}$$

The surface potential, **Φ**, can be obtained from Eq. I.24

$$\frac{\Phi}{q_M RT} = -\frac{1}{\alpha}\frac{E^o}{RT}\Gamma\left[\frac{1}{\alpha},-\mathrm{Ln}(\theta)\right] = -\frac{1}{\alpha}\frac{E^o}{RT}\Gamma\left[\frac{1}{\alpha},\left[-\frac{RT}{E^o}\mathrm{Ln}(\Pi)\right]^{\alpha}\right], \qquad \text{(Eq. VII.17)}$$

where **Γ** is the *Gamma* function, $\Gamma(a,z) = \int_z^{\infty} t^{a-1} e^{-t}\,\delta t$. According to Eq. VII.17, the surface potential is negative for $\forall\theta \le 1$ and reaches its maximum value for $\theta = 1$ (or $\Pi = 1$)

$$\left.\frac{\Phi}{q_M RT}\right|_{\theta=1} = -\frac{1}{\alpha}\frac{E^o}{RT}\Gamma\left(\frac{1}{\alpha},0\right) \qquad \text{(Eq. VII. 18)}$$

The integral free energy of the adsorbed phase, $\Delta\overline{G}^a$, can be obtained from Eq. VII.6 for a perfect gas

$$\frac{\Delta\overline{G}^a}{q_M RT} = -\frac{1}{\alpha}\frac{E^o}{RT}\left\{\Gamma\left[\frac{1}{\alpha},-\mathrm{Ln}(\theta)\right] + \theta\,\alpha\left[-\mathrm{Ln}(\theta)\right]^{1/\alpha}\right\} \qquad \text{(Eq. VII.19)}$$

The integral free energy of the adsorbed phase is always negative and reaches its maximum value when $\theta = 1$ (or $\Pi = 1$), which equals the surface potential:

$$\left.\frac{\Delta\overline{G}^a}{q_M RT}\right|_{\theta=1} = \left.\frac{\Phi}{q_M RT}\right|_{\theta=1} = -\frac{1}{\alpha}\frac{E^o}{RT}\Gamma\left(\frac{1}{\alpha},0\right) \qquad \text{(Eq. VII.20)}$$

The integral free energy relative to saturation, Ψ, can be obtained by subtracting Eq. VII.20 to Eq. VII.19

$$\frac{\Psi}{RT} = -\frac{1}{\alpha}\frac{E^o}{RT}\left\{\Gamma\left[\frac{1}{\alpha},-\mathrm{Ln}(\theta)\right] - \Gamma\left(\frac{1}{\alpha},0\right) + \theta\,\alpha\left[-\mathrm{Ln}(\theta)\right]^{1/\alpha}\right\} \qquad \text{(Eq. VII.21)}$$

It should be highlighted that the integral free energy relative to saturation is always negative and it reaches its maximum value when $\theta = 0$ (or $\Pi = 0$), which equals both the surface potential and the integral free energy of the adsorbed phase at $\theta = 1$ (or $\Pi = 1$):

$$\left.\frac{\Psi}{RT}\right|_{\theta=1} = \left.\frac{\Delta\overline{G}^{a}}{RT}\right|_{\theta=1} = \left.\frac{\Phi}{q_M\,RT}\right|_{\theta=1} = -\frac{1}{\alpha}\frac{E^o}{RT}\Gamma\left(\frac{1}{\alpha},0\right) \qquad \text{(Eq. VII.22)}$$

Furthermore, the integral free energy relative to saturation when $\theta = 0$ (or $\Pi = 0$) coincides with the value of $-G^o$ defined in Eq. VII.15, that is:

$$G^o = -\left.\frac{\Psi}{RT}\right|_{\theta=0} = \frac{1}{\alpha}\frac{E^o}{RT}\Gamma\left(\frac{1}{\alpha},0\right) \qquad \text{(Eq. VII.23)}$$

On the other hand, the representation of $-\Psi/RT$, calculated by Eq. VII.15 and by the Dubinin-Astakhov isotherm (Eq. VII.21) with $Z = -1/Ln(\Pi)$ in double logarithmic axes for $E^o/RT > 10$ in the Π interval 10^{-5} – 10^{1} follows a linear trend with slope $-(\alpha+1)$. Accordingly:

$$m = (\alpha+1) \qquad \text{(Eq. VII.24)}$$

The energy $\mathbf{E^o}$ is restricted to values >10 RT, so that the plateau zone does not appear in the representation of the isotherm. It should be noted that the plateau zone tends to higher Π values with the reduction of energy E^o, being the adsorption practically negligible when $E^o \rightarrow$ RT. For instance, for $E^o/RT = 1$, $\alpha = 2$ and $\Pi = 0.1$, $\theta < 5 \times 10^{-3}$ (most of the adsorption has occurred at $\Pi = 0.1$ for most of the microporous materials).

Finally, the value of **k** can be determined in terms of the Dubinin-Astakhov isotherm by equaling the integral free energy relative to saturation calculated by this isotherm for $Z = -1/Ln(\Pi) = 1$ and that derived from the PTI presented in this work (Eq. VII.15) for the same Π value, $G^o/(1+k)$. The value satisfied by this equation is expressed by Eq. VII.25

$$k = \frac{1}{\dfrac{\dfrac{E^o}{RT}\dfrac{\Gamma\left(\frac{1}{\alpha},0\right)}{\alpha}}{\dfrac{1}{\exp\left[\left(\frac{E^o}{RT}\right)^{-\alpha}\right]} + \dfrac{E\left[\frac{\alpha-1}{\alpha},\left(\frac{E^o}{RT}\right)^{-\alpha}\right]}{\alpha}} - 1} \qquad \text{(Eq. VII.25)}$$

where $E[n,z]$ is the integral exponential function:

$$E[n,z] = \int_t^{\infty} \frac{\exp(-z\,t)}{t^n}\delta t \qquad \text{(Eq. VII.26)}$$

In order to assess that the Dubinin-Astakhov isotherm fits to the isotherm proposed in this work, Figure VII.19 plots the integral free energy relative to saturation, $-\Psi/RT$, calculated according to both isotherms for the Π range 10^{-5} – 0.97 with the parameters determined from Eqs. VII.23-VII.25 for α = 1.5, 2.0 and 2.5 and E^o = 5 RT and 20 RT.

VII.2.3. Comparison between the PTI and the Langmuir isotherm

Although the surface thermodynamics approach (2D) does not seem to be adequate to describe the equilibrium adsorption process in microporous materials, the generalized Langmuir isotherm (LG) (Eq. VII.27 or I.4) will be taken into account in this section because it has been widely used in many studies that describe the adsorption process in microporous materials (e.g., zeolites):

$$q(P) = \int_{E_{min}}^{E_{max}} q_L(P,E)\chi(E)\delta E \qquad \text{(Eq. VII.27)}$$

$$\text{with } \theta = \left(\frac{y}{1+y}\right)^{\beta} \text{ and } y = (K\,P)^{\delta} \exp\left(-\delta\frac{\Delta H}{RT}\right) \qquad \text{(Eq. VII.28)}$$

where **χ(E)** is the distribution function of adsorption energies, which takes values from the minimum energy, $\mathbf{E_{min}}$, to the maximum one, $\mathbf{E_{max}}$, **K** is the adsorption constant [kPa^{-1}], and ΔH is the enthalpy of adsorption [J mol^{-1}]. The surface potential, Φ, can be obtained by combining Eqs. I.24 and VII.28

$$\frac{\Phi}{q_M RT} = -\frac{y^{\beta}}{\delta}\int_0^t t^{\beta-1}(1+t\,y)^{-\beta}\,\delta t \qquad \text{(Eq. VII.29)}$$

Moreover, the integral free energy of the adsorbed phase, $\Delta\overline{G}^a$, can be obtained from Eq. VII.6 for a perfect gas

$$\frac{\Delta\overline{G}^a}{q_M RT} = \left(\frac{y}{1+y}\right)^{\beta} \mathrm{Ln}(\Pi) + \frac{\Phi}{q_M RT} \qquad \text{(Eq. VII.30)}$$

The integral free energy of the adsorbed phase is negative and increases with Π as the surface potential. Nevertheless, a maximum pressure value to account for adsorption saturation, P^o [kPa], has to be fixed. In principle, a value for θ = 0.99999 is high enough to assume that the pressure is practically the saturation vapor pressure. For this value of θ, Eq. VII.31 is obtained

$$P^o = \frac{\left(\dfrac{1}{(0.99999)^{-1/\beta}-1}\right)^{1/\delta} \exp\left(\dfrac{\Delta H}{RT}\right)}{K} \qquad \text{(Eq. VII.31)}$$

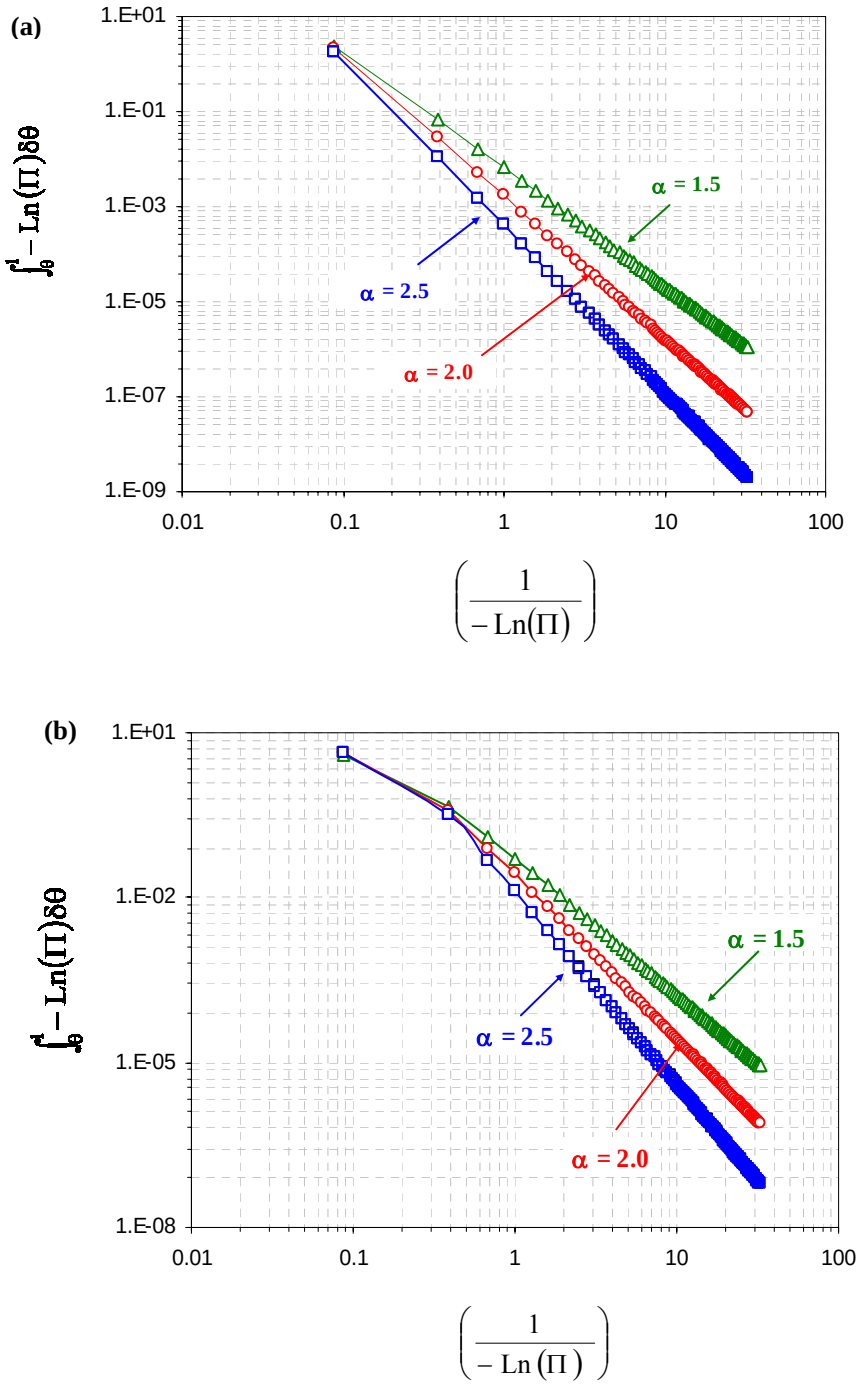

Figure VII.19: Integral free energy relative to saturation, Ψ/RT, calculated by the Dubinin-Astakhov isotherm (points) and by the isotherm proposed in this work with the parameters calculated by Eqs. VII.23-VII.25 (straight lines). The Π values analyzed are in the range 10^{-5} – 0.97 for α = 1.5, 2.0 and 2.5. (a) E^o = 20 RT, (b) E^o = 5 RT.

However, it should be noted that if other values of θ are taken into account, the value for ΔG^o at $P = P^o$ will be different. For instance, for $\beta = \delta = 1$ (single-site Langmuir isotherm) when θ = 0.999, 0.99999, 0.9999999, $-\overline{\Delta G}^a/q_M$ = 6.908 RT, 11.513 RT, and 16.118 RT, respectively. Obviously, because the Langmuir isotherm admits infinite pressure values, the value of the integral free energy of the adsorbed phase can increase indefinitely. On the other hand, the integral free energy relative to saturation, Ψ, can be calculated by Eq. VII.32

$$\frac{\Psi}{RT} = -\frac{y_o^{\beta}}{\delta}\int_0^t t^{\chi-1}\left(1+t\,y_o\right)^{-\beta}\,\delta t - \left(\frac{y}{1+y}\right)^{\beta}\ln(\Pi) - \frac{\Phi}{q_M\,RT} \qquad \text{(Eq. VII.32)}$$

$$y_o = \frac{1}{(0.99999)^{-1/\beta} - 1}$$

The representation of $-\Psi/RT$ with $Z = 1/\mathrm{Ln}(\Pi)$ for the single-site Langmuir isotherm ($\beta = \delta = 1$) does not show the potential trend suggested by the PTI presented in this work for any pressure range. Figure VII.20 shows the evolution of $-\Psi/RT$ with **Z** for several P^o values for the generalized Langmuir isotherm. As can be seen, the tend of $-\Psi/RT$ with **Z**

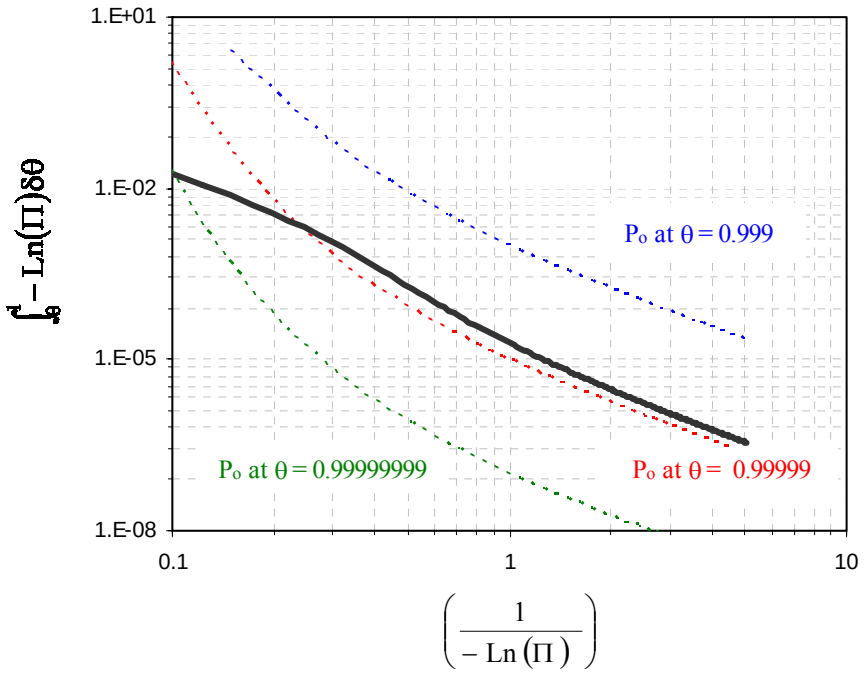

Figure VII.20: Integral free energy relative to saturation, Ψ/RT, calculated by the Langmuir isotherm as a function of parameter Z = 1/-Ln(Π) for Π values in the range 10^{-4} – 0.90. The dashed lines correspond to the single-site Langmuir isotherm ($\beta = \delta = 1$) calculated for P^o at θ = 0.999, 0.99999 and 0.9999999, while the straight line corresponds to the generalized Langmuir isotherm with $\beta = 0.00025$ and $\delta = 1.5$.

becomes potential depending on the values of β and δ and on the pressure range. Figure VII.21 plots $-\Psi/RT$ with **Z** for the interval $0.001 < \Pi < 0.50$ and P^o calculated at $\theta = 0.99999$, and for the specific β and δ values that allow a potential behavior.

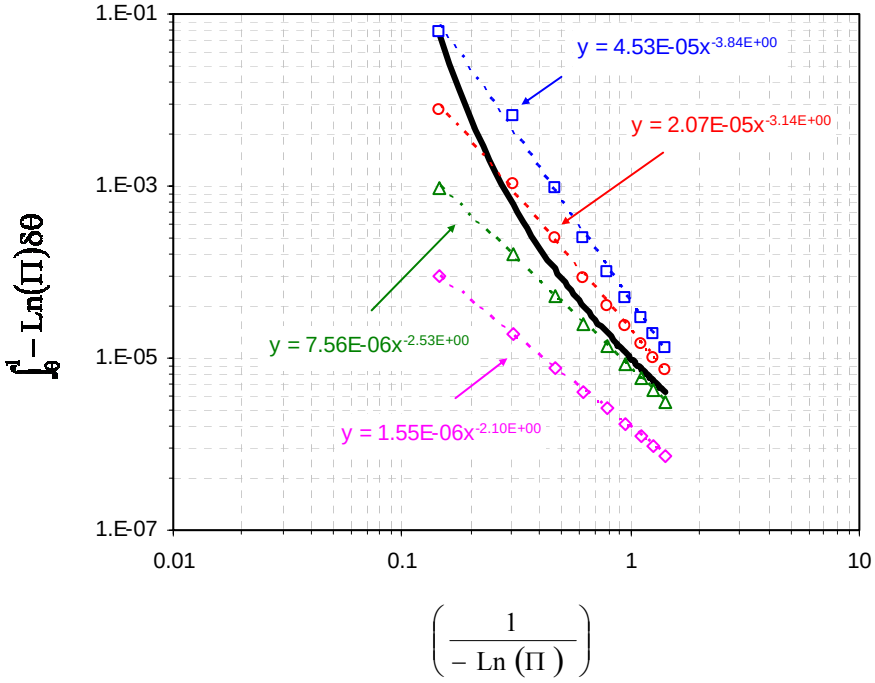

Figure VII.21: Integral free energy relative to saturation, Ψ/RT, calculated by the Langmuir isotherm as a function of parameter Z = 1/-Ln(Π) for Π values in the range 10^{-3} – 0.50 and P^o calculated at θ = 0.99999. The points correspond to the values calculated by the generalized Langmuir isotherm: □ (β = 0.0015, δ = 2.0), ○ (β = 0.00025, δ = 1.5), △ (β = 0.000045, δ = 1.0), and ◇(β = 0.000008, δ = 0.5). The dashed lines correspond to potential fittings (Eq. VII.15), while the straight line corresponds to the single-site Langmuir isotherm (β = δ = 1), whose behavior in non-potential.

Therefore, the generalized Langmuir isotherm allows to explain the potential trend for the integral free energy relative to saturation, **Ψ**, with parameter **Z** only for particular pressure intervals. The exponent of the PTI, which constitutes the parameter that characterizes the structure of the adsorbent, does not depend on the values of β and δ in an easy way. This observation contrasts with the potential trend observed for the Dubinin-Astakhov isotherm, which persists for practically all the reduced pressure interval (except for very low pressures, where adsorption is not important), and whose exponent is simply **-(α + 1)**. These remarks allows us to conclude that, despite being widely used in the literature and in this work (see section VII.1 for the description of the unary and binary adsorption of water and ethanol vapors on zeolite NaA powder), the Langmuir isotherm is not the most proper isotherm to

describe the adsorption process in microporous materials, because it actually deals with a 3D process instead of 2D on which it was originally focused.

VII.2.4. Characterization of active carbons and zeolites by the PTI

A series of active carbons and zeolites that can be used for gas and vapor adsorption have been used to test the suitability of the PTI to characterize microporus materials. It should be noted that the active carbons that are used to adsorb gases and vapors are usually those with the best quality (higher surface area). The active carbons might be impregnated with some species to improve their ability of adsorbing certain gases. The active carbons and zeolites characterized in this section were commercially supplied, whose main characteristics are summarized, respectively, in Tables VII.10 and VII.11. The experimental data for the active carbons were obtained from *Llorens (2005)*, while those for zeolites were determined in the present work. The active carbons were formerly characterized in terms of humidity, fly ash, pH, and adsorption of carbon tetrachloride. Moreover, the active surface area, pore volume and mean pore size for all the active carbons and zeolites were characterized by N_2 adsorption at 77 K. For further details see section III.4.6. It should be noted that the adsorption and desorption curves of N_2 at 77 K for all the active carbons and zeolites are coincident and only show hysteresis beyond $\Pi = P/P^o = 0.75$ (see for instance Figure VII.22 for ZSM-5), which confirms the microporous character of these materials. Morever, for the fittings to the PTI, all the active carbons and zeolites were also subjected to characterization by the adsorption of N_2 at 77 K for the reduced pressure ($\Pi = P/P^o$ [-]) range of, respectively, 10^{-2} – 0.99 and 10^{-7} – 0.99.

Figures VII.23 and VII.24 show the adsorption isotherms of N_2 at 77 K for the active carbon ABEK and for faujasite, respectively, together with their fittings to the PTI. It can be observed that the potential trend is not preserved for all the range of reduced pressures ($\Pi = P/P^o$) range surveyed, which shows that the integral free energy relative to saturation, $-\Psi/RT$, as a function of $1/-Ln(\Pi)$, changes as the pores of the adsorbent are progressively filled. However, a more thorough analysis reveals that the change in the slope, **m**, is observed beyond 90% of surface coverage, that is, for $-Ln(\Pi) \approx 1.4$ or $\Pi = P/P^o \approx 0.25$. Because the interest of these adsorbents relies on their micropores, which are filled beyond 90% of surface coverage, the value of **m** has been calculated for the interval of reduced pressures 10^{-4} – 0.25.

Tables VII.12 and VII.13 show the values of **m** found from the fittings of experimental adsorption data of N_2 at 77 K to the PTI, respectively, for the active carbons and zeolites surveyed in this study. The details concerning the fittings can be found in Appendix D. As can be seen in Table VII.12, the values of **m** for all the active carbons are very similar and

Table VI.10: Active carbons characterized by the PTI from N_2 adsorption at 77 K. Experimental data obtained from *Llorens (2005)*.

Sample	*Humidity [wt.%]*	*Fly ashes [wt.%]*	*pH [-]*	*ATC [wt.%]*	*BET surface area*[3] *[m^2 g^{-1}]*	*Micropore volume*[4] *[cm^3 g^{-1}]*	*Mean pore size*[4] *[nm]*	*Supplier*
ABEK[1,2]	17.14	15.66	6.08	70	1135	0.288	2.9	Picactif
BPL	2.85	6.63	7.16	68	1232	0.342	3.6	Aguas de Levante
GH12132	5.77	2.77	9.61	45	953	0.310	3.2	Aguas de Levante
GH6112	6.09	2.14	9.43	39	843	0.272	3.2	Warwick Benbassat
GMA	3.86	2.77	9.36	67	1294	0.408	3.3	-
HRO[1]	4.89	2.66	9.74	49	1021	0.334	3.2	Betaquimica
PANRG	12.47	1.70	9.25	25	784	0.218	3.8	Panreac
RBAA1[2]	2.30	18.40	9.88	42	862	0.245	3.4	Norit
RGB[1,2]	17.60	9.18	9.20	73	1331	0.403	3.2	Betaquimica
RGG08[2]	3.45	15.42	8.74	72	1222	0.325	3.4	Norit
RGK[2]	22.58	9.04	6.84	64	1179	0.345	3.5	Betaquimica
RZN1[2]	9.84	13.69	5.73	57	1087	0.339	3.4	Norit
TA[1]	2.59	3.02	9.80	85	1451	0.407	2.7	Picactif

[1] Activated with water vapor

[2] Impregnated

[3] Determined from a N_2 adsorption isotherm at 77 K by the BET technique

[4] Determined by theBarret, Joyner and Halenda method (BJH) from N_2 adsorption data at 77 K

Table VII.11: Zeolite powders characterized by the PTI from N_2 adsorption at 77 K.

Sample	*Density* [2] *[g cm^{-3}]*	*BET surface area* [3] *[m^2 g^{-1}]*	*Micropore volume* [4] *[cm^3 g^{-1}]*	*Particle size (mean) [μm]*	*Micropore size* [7] *[nm]*	*Supplier*
Zeolite NaA	2.01	255	0.100	2.0 [5]	0.41	IQE
Faujasite [1]	2.34	611	0.217	-	0.86	-
Zeolite NaX	1.96	716	0.273	1.2 [5]	0.74	Fluka
H-Beta	2.34	632	0.215	8.1 [6]	0.65 x 0.56 0.75 x 0.57	
Ca-ZSM-5	1.99	474	0.145	-	0.53 x 0.55 0.51 x 0.56	Tosoh
Na-Mordenite	2.26	279	-	-	0.65 x 0.70 0.26 x 0.57	Tosoh

[1] Sample supplied by the Federal Institute for Materials Research and Testing (BAM, Unter den Eichen 87, 12205-Berlin, Germany.

[2] Determined by an He picnometer

[3] Determined from a N_2 adsorption isotherm at 77 K by the BET technique

[4] Determined by the Horvath-Kawazoe method from a N_2 adsorption data at 77 K

[5] Determined by photon correlation spectroscopy (PCS)

[6] Determined by TEM

[7] From *Breck (1984)*

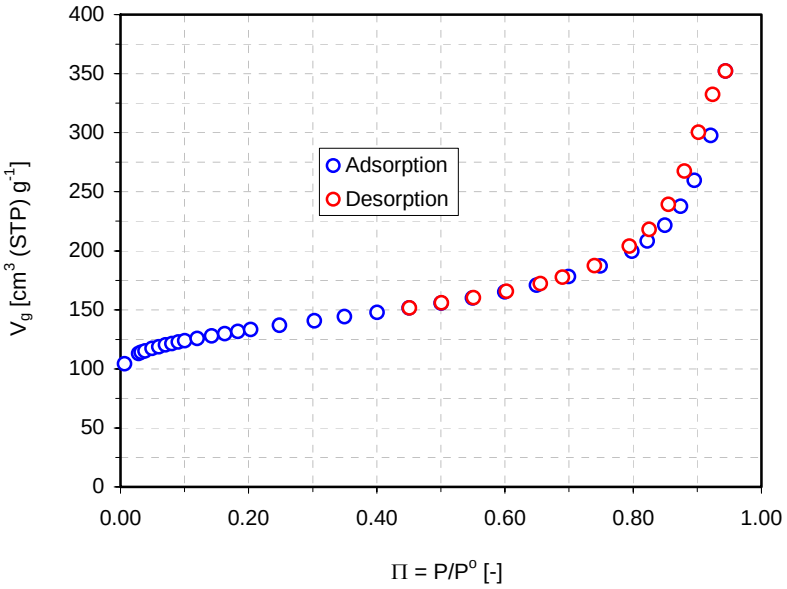

Figure VII.22: Adsorption and desorption isotherms of N_2 at 77 K for zeolite ZSM-5 (see Table VII.10). Hysteresis is only observed for $\Pi = P/P^o > 0.75$.

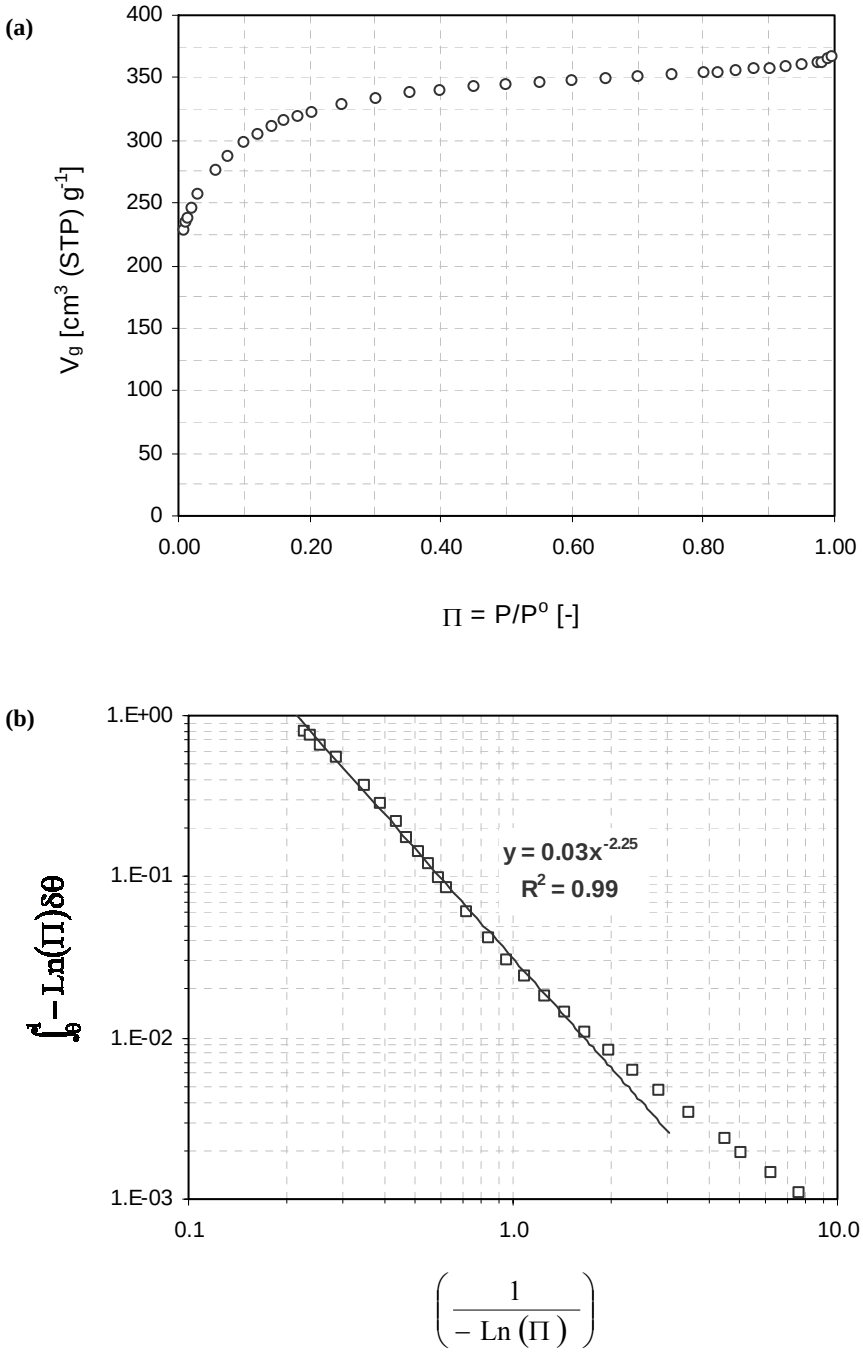

Figure VII.23: (a) adsorption isotherm of N_2 at 77 K for the active carbon ABEK (see Table VII.10), and (b) representation of the PTI in terms of Eq. VII.15.

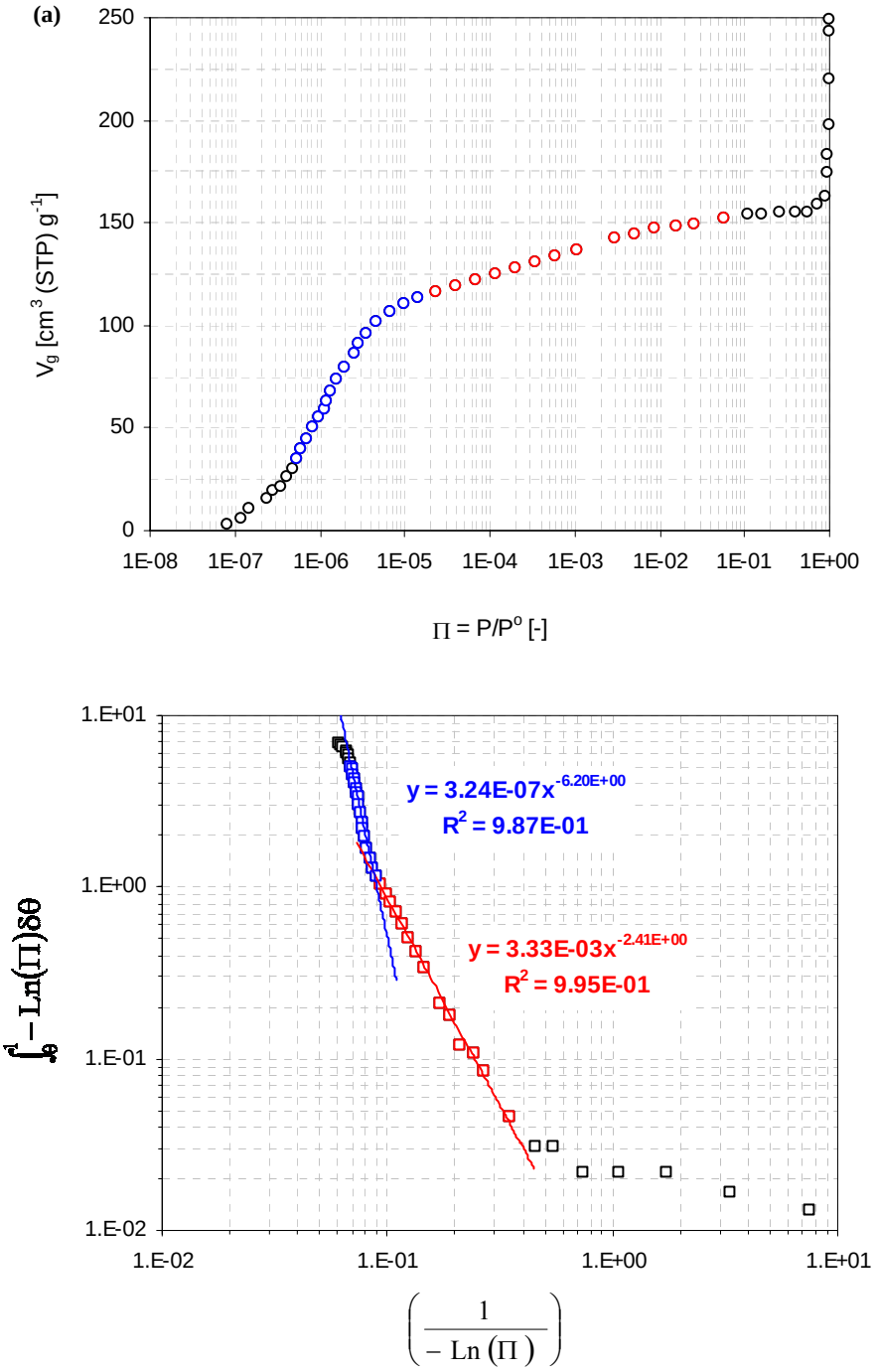

Figure VII.24: (a) adsorption isotherm of N_2 at 77 K for faujasite (see Table VII.11), and (b) representation of the PTI in terms of Eq. VII.15.

Table VII.12: Active carbons characterized by the PTI

Number	***Sample***	***m [-]*** [1,2]	***r^2 [-]***
1	**ABEK**	2.25 ± 0.11	0.9943
2	**BPL**	2.23 ± 0.06	0.9988
3	**GH12132**	2.10 ± 0.06	0.9985
4	**GH6112**	1.88 ± 0.04	0.9994
5	**GMA**	2.20 ± 0.13	0.9965
6	**HRO**	1.98 ± 0.08	0.9973
7	**PANRG**	1.21 ± 0.02	0.9995
8	**RBAA1**	2.24 ± 0.10	0.9974
9	**RGB**	2.06 ± 0.16	0.9915
10	**RGG08**	2.36 ± 0.07	0.9984
11	**RGK**	2.17 ± 0.12	0.9956
12	**RZN1**	2.37 ± 0.09	0.9978
13	**TA**	2.87 ± 0.03	0.9999

[1] Determined for a confidence interval of 95%.

[2] Fittings in the Π range 0.0300 – 0.2500.

Table VII.13: Zeolites characterized by the PTI

Number	***Sample***	***m_1 [-]*** [2,3]	***r_1^2 [-]***	***m_2 [-]*** [2,4]	***r_2^2 [-]***
14	**Zeolite A**	7.27 ± 2.60	0.9376	1.52 ± 0.46	0.9733
15	**Faujasite** [1]	6.20 ± 0.39	0.9869	2.41 ± 0.11	0.9948
16	**Zeolite X**	6.75 ± 2.56	0.9005	3.29 ± 0.11	0.9976
17	**Zeolite β**	3.99 ± 0.16	0.9931	1.36 ± 0.11	0.9750
18	**ZSM-5**	1.82 ± 0.30	0.9859	0.67 ± 0.02	0.9951
19	**Mordenite**	-	-	2.45 ± 0.13	0.9971

[1] Data supplied by the Federal Institute for Materials Research and Testing (BAM, Unter den Eichen 87, 12205-Berlin, Germany.

[2] Confidence interval for a probability level of 95%.

[3] Fittings in the Π range $5 \times 10^{-7} – 7 \times 10^{-5}$

[4] Fittings in the Π range $7 \times 10^{-5} – 0.2500$

approach the value of **2**, which reinforces the idea that this exponent captures the structural information related to the adsorbent. However, for the zeolites surveyed in this study, two different values of **m** (**m_1** and **m_2**) have been found, being the former higher than the latter. The first exponent, determined from the fittings in the Π range $5 \times 10^{-7} – 7 \times 10^{-5}$ might be related to the microporous framework of zeolites, while the latter might be ascribed to intercrystalline mesopores defined between adjacent zeolite particles. Figure VII.25 shows the trend observed for exponent m_1 with respect to the molar SiO_2 /

Al_2O_3 ratio of the zeolites surveyed in this study. As can be observed, despite the experimental error in the determination of m_1 exponent for zeolites A and X listed in Table VII.13, a decreasing trend of this exponent with the molar SiO_2 / Al_2O_3 ratio appears to be observed. Therefore, according to Eq. VII.11, the adsorption of N_2 at 77 K at $\Pi < 10^{-5}$ seems to be higher for low Al_2O_3 zeolites with a 2D structure (e.g., ZSM-5) than for high Al_2O_3 zeolites with a 3D structure (e.g., zeolite A).

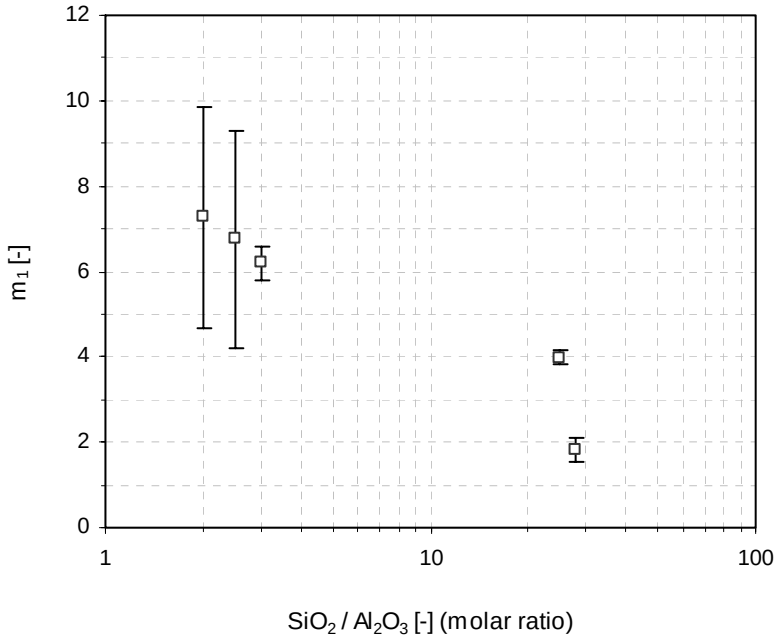

Figure VII.25: Trend observed for the exponent $\mathbf{m_1}$ with respect to the molar SiO_2 / Al_2O_3 ratio for the zeolites shown in Table VII.11. The SiO_2 / Al_2O_3 ratios were either provided by the supplier or were determined experimentally by XRF.

VII.3. FINAL REMARKS

In section VII.2, a new general expression has been developed from general concepts of solution thermodynamics (3D) that constitutes a useful tool to characterize the adsorption of gases and vapors on microporous materials (e.g., active carbons and zeolites). This isotherm has been defined as ***Potential Thermodynamic Isotherm (PTI)***, because it involves a potential trend between the integral free energy related to saturation $\mathbf{-\Psi/RT}$, and parameter $\mathbf{Z}$=1/-Ln(Π), where $\mathbf{\Pi}$ = P/P^o is the reduced pressure, θ is the fractional loading, and $\mathbf{m}$ is a structural paramenter that characterizes the adsorbent. In light of the results shown in section VII.2.4, microporous materials can be characterized from the adsorption isotherm of N_2 at 77

K through the use of the Potential Thermodynamic Isotherm. Parameter **m** derived from the PTI might be further used to predict the behavior of such materials to adsorb other gases and vapors (e.g., hydrogen).

Moreover, in light of the comments exposed in sections VII.2.2 and VII.2.3, the Dubinin-Astakhov isotherm can be deduced as a particular case of the PTI. However, the well-known single-site Langmuir isotherm cannot be fitted to the PTI, thus revealing that its 2D character is not proper to characterize the adsorption of gases and vapors in microporous materials. However, the single-site adsorption isotherm still constitutes a powerful tool to describe phenomenologically the unary adsorption of water and ethanol vapors on zeolite NaA powder according to the fittings shown in section VII.1. The single-site Langmuir isotherm can be extended to binary mixtures using the PRAS theory.